Monolithically 3-D Printed, Quadrupole Mass Filter for High-Precision, Compact, CubeSat Mass Spectrometry

by

Alejandro Diaz

B.S. Electrical Engineering and Computer Science, Concentration in
Latin American Studies and Environment and Sustainability
Massachusetts Institute of Technology, 2021

Submitted to the Department of Electrical Engineering and Computer Science
in partial fulfillment of the requirements for the degree of

Master of Engineering in Electrical Engineering and Computer Science

at the

MASSACHUSETTS INSTITUTE OF TECHNOLOGY

February 2023

Author . . . .
Department of Electrical Engineering and Computer Science
January 27, 2023

Certified by . . . .
Luis Fernando Velasquez-Garcia
Principal Research Scientist
Thesis Supervisor

Accepted by . . . .
Katrina LaCurts
Chair, Master of Engineering Thesis Committee

Monolithically 3-D Printed, Quadrupole Mass Filter for High-Precision, Compact, CubeSat Mass Spectrometry

by

Alejandro Diaz

Submitted to the Department of Electrical Engineering and Computer Science
on January 27, 2023, in partial fulfillment of the
requirements for the degree of
Master of Engineering in Electrical Engineering and Computer Science

Abstract

Mass spectrometry is the gold standard for quantitative chemical analysis. However, mainstream mass spectrometers are large, heavy, and power hungry, restricting their ability to be deployed into in-situ, portable, and hand-held scenarios, e.g., drones and CubeSats (measurements in the atmosphere are crucial for monitoring climate change). Miniaturization has been attained at the expense of great loss in performance, caused in part by fabricating non-ideal electrode shapes and having low relative assembly precision. Via additive manufacturing, it is possible to create complex objects, e.g., mass filters with better shaped and spatially arranged electrodes. We report the design, fabrication, and characterization of the first, monolithically 3D-printed, hyperbolic, compact RF quadrupole mass filters. The devices were made using an advanced, multi-material extrusion printer. The devices are tested as RF-only collision cells for use in miniaturized triple quadrupole mass spectrometers and as quadrupole mass filters for miniaturized mass spectrometers (we detected argon at a resolution of 5 and 1-250 amu mass range). We also developed compact electronics to drive the quadrupoles that are compatible with the size, weight, and power constraints of deployable platforms, such as CubeSats ($<$3W, up to 400 V_{pp} sinusoidal amplitude, 1-3MHz, $>$2000 voltage steps for 100:1 resolution). This work provides an opportunity for more precise, low-power, deployable, and compact mass spectrometry systems.

Thesis Supervisor: Luis Fernando Velasquez-Garcia
Title: Principal Research Scientist

Acknowledgments

First, to my advisor, Luis Fernando Velasquez-Garcia, thank you for the constant support and the opportunity to work on an incredible project. It all started with taking 6.UAT (Oral Communication Class) and having you as my recitation instructor. Now I am here finishing up the MEng. Without your feedback and guidance this project would not have come to fruition. Thank you for being a great advisor and mentor.

To my colleagues for all their good company and help! To Nicholas K. Lubinsky for always lending a helping hand in lab, whether it was with vacuum setup or metal plating or last minute formula questions :). I couldn't have done this thesis without your help. To Jorge Canada for all of the help in lab with the 3D-printing and characterization. Not to mention a little Spanish conversation sprinkled in. To Zoey Bigelow for always being a bright ray of sunshine and someone to bounce ideas off of. To Colin Eckhoff for all of the help with the theory, setup and circuitry. To Alex Kashkin for the good vibes and social planning. To Hyeonseok Kim for keeping our lab running and the amazing food! To Hanjoo Lee for all the good company, advice, and good vibes in the lab! To Javier Izquierdo Reyes for all the good times and advice, even from afar in Mexico.

To my academic advisor and teacher Gim Hom for being such a cool dude and always having my back as a student and when I've been picking classes and internships. I wish you the absolute best. Thank you to all of my teachers throughout my life, I really am the product of my teachers.

To pika, for being such a warm and welcoming place and being my home while I completed my MEng. I am here, in the skylight room of pika writing these words, hours before turning in this thesis. I am sad to leave this house with all the friends and memories and warm feelings, but I am so glad for all the positive experiences I've had here. Everyone is so cool and I hope to see everyone in the future!

To all my friends, both in the area and elsewhere, you've made it all worth it and made it possible for me to call Boston home for the past few years. I've had my ups and downs and I am so glad to have had you by my side—whether you are friends from high school, MIT, pika, The Chorallaries of MIT, climbing (lol) or travels abroad. You have made it all worth it and helped me back up when I stumbled.

Lastly, to my family, I am nothing without you and I love you all so very much! Thank you Mama and Papa! Also thank you so much for helping me with the final revision! You have always supported me and are always there when I need it. Thank you Isabella! I am so proud of you and couldn't have asked for a more caring and loving sister! I am so excited to see where the future takes you and I will always be here to cheer you on and help you out! Thank you to Cesar Diaz for being an older brother to me and my grandparents on both sides for being so caring. Thank you to all of my aunts and uncles and cousins for always having my back and cheering me on.

I am excited for the next chapter and I know that you all will continue to be in my life and push me forwards.

Thank you.

Contents

List of Figures

List of Tables

Chapter 1 Introduction

Mass spectrometry is the gold standard for quantitative chemical analysis. Mass spectrometers employ mass filters that generate electromagnetic fields to sort out (in vacuum, by mass-to-charge ratio) the ionized constituents of a sample [1.1]. However, mainstream mass spectrometers are large, heavy, and power hungry, restricting their ability to be deployed into in-situ, portable, and hand-held scenarios, e.g., drones, CubeSats. This makes the history of precise, in-situ atmospheric measurements in space limited and an area for growth. These measurements are crucial for monitoring climate change and tracking pollution [1.2].

Some of the most popular mass spectrometry technologies are magnetic sector, time-of-flight (TOF), and quadrupole field. As mass spectrometers get smaller, magnetic sector mass spectrometry requires larger, more powerful magnets and TOF mass spectrometry requires high performance electronics to measure increasingly shorter ion flight times—this makes **quadrupole field mass spectrometry** the natural solution for miniaturization [1.3]. A diagram of a quadrupole mass filter within a mass spectrometer setup is shown below. As the name suggests, a quadrupole mass filter is constructed with four conductive rods. These rods filter ions of certain mass when sinusoids of specific phase, amplitude, and DC offset are applied across the rods.

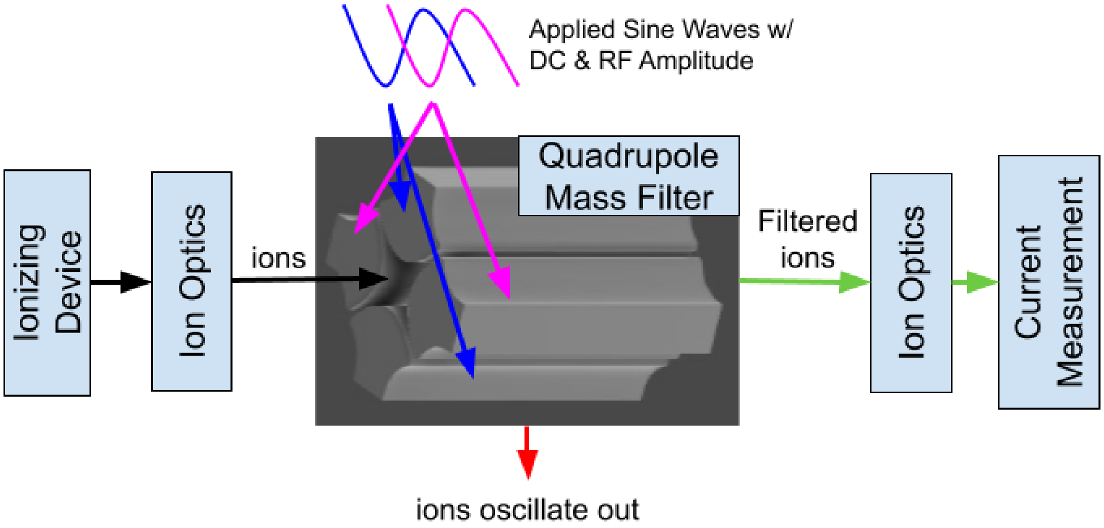

Figure 1-1: Quadrupole Mass Spectrometer Diagram. Ion optics direct and focus the ions.

However, there are challenges to miniaturization. Historically, miniaturization has been attained at the expense of great loss in performance, caused in part by fabricating non-ideal electrode shapes (normally circular rods instead of the ideal hyperbolic rods for ease of manufacturing) and having low relative assembly precision [1.4].

Recent research for the miniaturization of mass spectrometry often meets one or two of the following: low-power, low-cost, compact, hyperbolic rods, or ease of manufacturing. However, we achieve all of these factors and fill the clear gap in miniature mass spectrometry [1.5]. Via additive manufacturing, it is possible to create monolithically and more precisely, complex objects, e.g., mass filters with better shaped (specifically hyperbolically shaped) and spatially arranged electrodes. Also, additive manufacturing is compatible with in-space manufacturing (it is very expensive to put a mass in orbit; 3D printing greatly reduces material waste and is a powerful multi-purpose manufacturing tool in space [1.6]).

In this thesis we monolithically manufacture a quadrupole mass filter that we demonstrate as both a collision cell (for use in a triple quad—one of the most powerful mass spectrometers is a triple quad [1.7]; the instrument uses two quadrupole mass filters in tandem with a collision cell, that is a quadrupole run with only RF) and as a standalone quadrupole mass filter. There are reports of 3D-printed quadrupoles

[1.8], but they are not monolithically made.

In parallel we developed compact, low-power (<3 W), precision electronics for driving the quadrupole with two 180 degree out-of-phase sinusoidal waves (these sinusoids can be varied and increased up to 400 V_{pp}—volts peak to peak). The driving frequency can be varied up to 3 MHz (the goal was 1-3 MHz).

1.1 Background

1.1.1 Mathieu Equations of Ion Movement

To understand the movement of the ions within the quadrupole mass filter and filter for only ions of certain mass, we need to understand the equations that govern the movement of the ions. The ion movement through the quadrupole rods is given as a function of x and y coordinates, frequency, and the potentials across the electrodes (which are a function of the DC and RF voltages applied). Through substitution we put these equations in the form of the Mathieu Equation below [1.3].

$$\frac{d^2u}{d\xi^2} + (a - 2qcos(2(\xi - \xi_0)))u = 0$$

We then arrive at the following equations for the parameters a and q (dimensionless parameters that determine whether the trajectories of the ions are stable—we use a=.23 and q=.7) [1.3]. m is the ion mass (amu), e is the charge of the electron (assumed to be 1 for most cases), and r_o is the radius between the hyperbolic rods that constitute the quadrupole mass filter (cm)[1.9]. U is the DC potential acting on the electrodes and V is the amplitude of the RF sinusoidal potential acting on the electrodes, with angular velocity ω=2πf, where f is the RF frequency (MHz).

$$a = \frac{8 * e * U}{m * r_0^2 * \omega^2} \tag{1.1}$$

$$q = \frac{4 * e * V}{m * r_0^2 * \omega^2} \tag{1.2}$$

By keeping constant the dimensionless parameters while varying the bias voltages, it is possible to scan across a wide range of masses. A visual example in the form of a plot can be seen in Fig. 1-2 (the solutions for both x and y in the cartesian plane define the stable region for ions of specific mass) [1.3]. Using the Mathieu equation, one can specify the dimensions, driving voltages, mass range, and resolution of a given quadrupole. By operating the quadrupoles in the second stability region (not shown in Fig. 1-2), it is possible to attain even higher resolution at the cost of higher driving amplitudes. Other possibilities for improving the performance of the mass filter include signal processing [1.10].

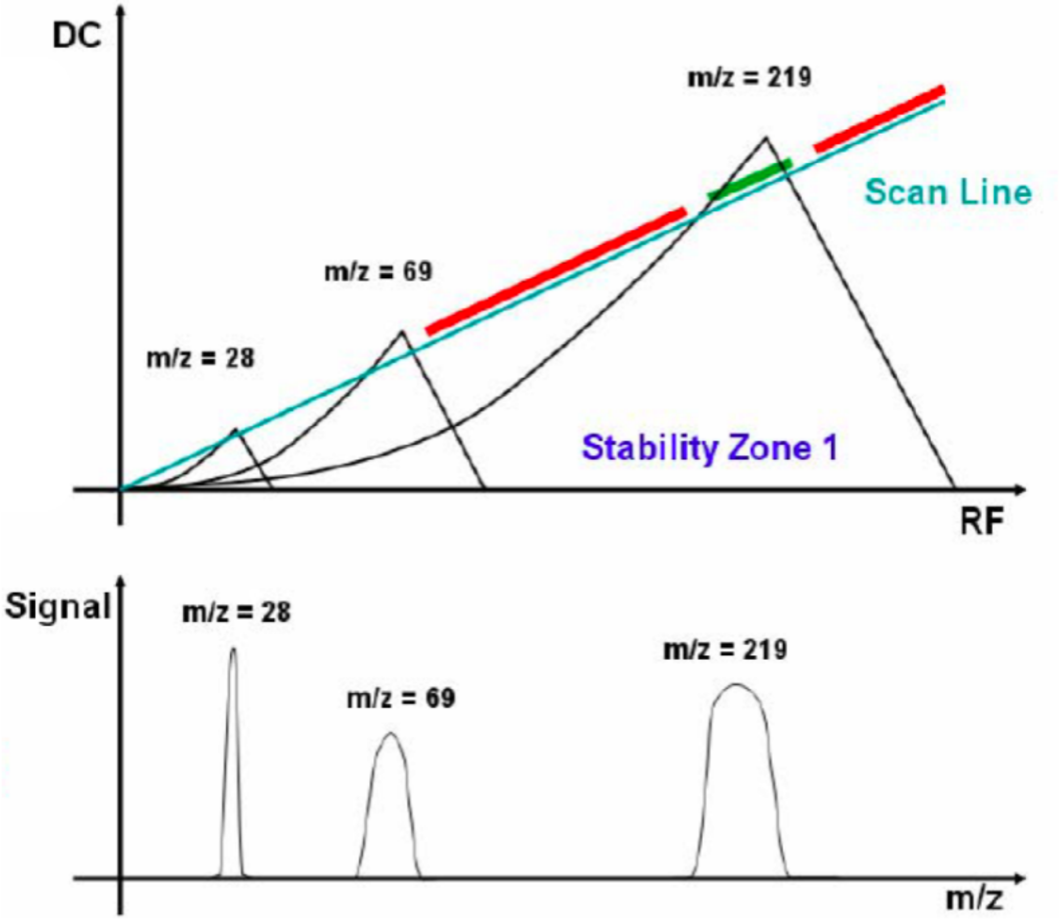

Figure 1-2: Stability Regions for a quadrupole as a function of applied DC and RF amplitudes [1.3]. The stable regions for the X and Y directions for three different masses are shown. The scan line in green is arbitrarily chosen; however, for greatest resolution of peaks, the portion of the stability zone that is intersected by the scan line should be minimized. The lower graph shows how the length of stability zone intersected impacts the peak resolution.

As shown above, resolution of the mass spectrum is affected by the scan line and its intersection with each stability zone. However, resolution is more thoroughly defined below.

1.1.2 Quadrupole Mass Filter Resolution

The resolution of a mass spectrum for a quadrupole mass filter is a function of h (a constant determined by a and q—for 1st stability region $h = 15$), L (quadrupole length in cm), f (frequency in MHz), m (amu), v_z (axial ion velocity), e_z (ion region energy— ∼10 eV in our case) and e (assumed to be 1) [1.3].

$$R = \frac{1}{h} \ * f^2 * L^2 * \left(\frac{m}{2 * v_z * e} \right) \tag{1.3}$$

$$v_z = \left(\frac{2 * e_z}{m} \right)^{\frac{1}{2}} \tag{1.4}$$

This resolution equation, along with the a and q equations as a function of the DC and RF amplitudes, will be very important throughout the paper. A script to calculate these values is in the git repository linked in the appendix.

1.1.3 Summary of Thesis

We developed compact, monolithically 3D-printed, RF quadrupole mass filters via extrusion, using PLA (Polylactic Acid—dielectric parts) and PLA doped with copper nano-particles (conductive parts—called Electrifi by manufacturer). The quadrupole rods are the ideal hyperbolic shape [1.11] with a 4 mm diameter aperture. The longer the quadrupole, the better the resolution (Eqn. 1.3), but because of the volume constraints of a CubeSat, the quadrupole cannot be longer than 12 cm. We tested 7.5 cm and 10 cm quadrupoles. The rods are designed for 1-3 MHz frequency, although higher frequencies would have better resolution (Eqn. 1.3), at the expense of higher power requirements and more sophisticated electronics. The rods are designed for RF amplitude voltages up to 400 V_{pp}; however, higher voltages would allow a larger mass scan range (Eqn. 1.1, 1.2). We also explored ideas for improving the performance of the mass filter, such as increasing the length, and varying the frequency. We achieved a resolution of 5 across a 1-250 amu mass range for the measurement of argon at 40 amu with the 7.5 cm quadrupole mass filter. There were also promising results for the detection of FC-43 (Ch. 4),

In parallel we developed compact, low-power, precision electronics for driving the quadrupole with two 180 degree out-of-phase sinusoidal waves . These sinusoids can be varied and increased up to 400 V_{pp} (>2000 voltage steps for 100:1 resolution). The driving frequency is 1-3 MHz and the electronics operate under 3 W (meeting CubeSat power requirements—nominally 10-30 W average payload power) [1.12]. For this project we focused on the requirements for a 6U CubeSat and wanted to leave room for other sensors and their power requirements.

1.2 Thesis Organization

Ch. 2 will cover the preliminary printing diagnostics and accuracy tests. Ch. 3 will describe the iterative design and manufacturing process of our monolithic quadrupoles—overcoming many printing problems. Ch. 4 will test these quadrupoles both as collision cells for a triple quad and as standalone quadrupole mass filters. Ch. 5 will pivot and describe the design, modeling, prototyping, and testing of the low-power electronics designed to work in tandem with the quadrupoles to produce mass spectra. Finally, Ch. 6 will discuss next steps and future work.

1.3 References

[1.1] Gross, Jürgen H. 2017. Mass Spectrometry. Cham: Springer International Publishing.

[1.2] Curtis D. Mowry, Russell L. Jarek, Jessica Román-Kustas, Amber C. Telles, Adam S. Pimentel, Gas Analysis by Mass Spectrometry, *Materials Characterization*, Vol 10, 2019 ed., *ASM Handbook*, ASM International, 2019, p 143–152, DOI:

10.31399/asm.hb.v10.a0006663

[1.3] Cheung, K. "Chip-Scale Quadrupole Mass Filters for a Micro-Gas Analyzer", 2009.

[1.4] Zhai, Y., Zhang, X., Xu, H., Zheng, Y., Yuan, T., & Xu, W. (2017). Mini Mass Spectrometer Integrated with a Miniature Ion Funnel. Analytical Chemistry, 89(7), 4177–4183. DOI: 10.1021/acs.analchem.7b00195

[1.5] Syms, R. R. A., & Wright, S. (2016). MEMS mass spectrometers: the next wave of miniaturization. Journal of Micromechanics and Microengineering, 26(2), 023001. DOI: 10.1088/0960-1317/26/2/023001

[1.6] Hirsch, M., McGuire, T., Parsons, M., Leake, S., & Straub, J. (2016). Enablement of scientific remote sensing missions with in-space 3D printing. In N. K. Dhar & A. K. Dutta (Eds.), Image Sensing Technologies: Materials, Devices, Systems, and Applications III (Vol. 9854, p. 985413). DOI: 10.1117/12.2223467

[1.7] Yost R. A. (2022). The triple quadrupole: Innovation, serendipity and persistence. Journal of mass spectrometry and advances in the clinical lab, 24, 90–99. DOI: 10.1016/j.jmsacl.2022.05.001

[1.8] P. Szyszka, J. Jendryka, M. Białas and T. Grzebyk, "Towards 3D printed compact Quadrupole mass spectrometer with MEMS components," 2021 IEEE 20th International Conference on Micro and Nanotechnology for Power Generation and Energy Conversion Applications (PowerMEMS), Exeter, United Kingdom, 2021, pp. 144-147, DOI: 10.1109/PowerMEMS54003.2021.9658391

[1.9] Wilamowski, B., et al., IECON'01. 27th Annual Conference of the IEEE Industrial Electronics Society (Cat. No.37243), "Enhancing The Sensitivity of Miniaturized Quadrupole Mass Spectrometers", DOI: 10.1109/iecon.2001.976470

[1.10] Cheung, K., Luis Fernando Velasquez-Garcia, & Akintunde Ibitayo Akinwande. (2009). Performance Enhancement Through Use of Higher Stability Regions and Signal Processing in Non-Ideal Quadrupole Mass Filters (United States 20090026363A1). Gauthier and Connors. `https://patents.google.com/patent/US20090026363`

[1.11] D. J. Gershman, B. P. Block, M. Rubin, M. Benna, P. R. Mahaffy, and T. H. Zurbuchen. Higher order parametric excitation modes for spaceborne quadrupole mass spectrometers. Rev. Sci. Instrum. 82, 125109 (2011). DOI: 10.1063/1.3669781

[1.12] EnduroSat, *6U CUBESAT PLATFORM*, accessed January 2023, `https://www.endurosat.com/cubesat-store/cubesat-platforms/6u-cubesat-platform/`.

Chapter 2 Printing Development and Characterization

In order to create monolithically printed, dual material quadrupoles, with both non-conductive and conductive material, we first had to find materials we could feasibly extrude in tandem.

We decided to use the standard PLA (Polylactic Acid) due to its ease of use and commercial availability. For the conductive filament we settled on Electrifi due to its low reported resistivity of .006 Ω*cm (lowest reported resistivity on the market at the time) [2.1].

In this chapter we will run some preliminary tests to verify the resistivity of the Electrifi filament and measure the precision of the Makergear M3-ID printer with respect to structures printed with both filaments. Ch. 3 continues experimentation with printing parameters and describes the iterative process used to attain monolithically manufactured quadrupoles.

2.1 Characterization of Filaments

2.1.1 Non-Conductive Filament—PLA

Tuning for the non-conductive filament was done by colleague Jorge Canada and the resulting parameters and accuracy tests are contained in the git repository referenced in the appendix.

2.1.2 Conductive Filament Resistivity

Conductivity and therefore resistivity is essential to the performance of the quadrupoles that we are manufacturing. Therefore, it is essential that we define the resistivity of the Electrifi filament that we use. We will define resistivity as the following:

$$resistivity = \Omega * cm$$

The given resistivity value by the manufacturer is .006 $\Omega * cm$ (for reference the resistivity of copper is 1.77 * $10^{-6} * \Omega * cm$); however, we found a resistivity of .03 $\Omega * cm$, which is about an order of magnitude higher. To measure this resistivity of .03 $\Omega * cm$, a long strip of Electrifi was printed, short copper leads were attached every .5 cm using silver epoxy, and then a current of .1 A was applied across the Electrifi. The voltage was then measured relative to ground every .5 cm using the copper leads. Silver paste was used for connections to the Electrifi prints as it has the lowest contact resistance—in the realm of .5 Ω according to the manufacturer (vs. screw terminals or melted Electrifi) [2.2].

*D*istance (cm)	Voltage Measured (mV)	Resistance (Ω)	Resistance per .5 cm (Ω)
0.5	28.0	.28	.06
1.0	34.0	.34	.065
1.5	40.5	.405	.053
2.0	45.8	.458	.064
2.5	52.2	.522	.054
3.0	57.6	.576	

Table 2.1: Resistance tests every .5 cm of printed Electrifi Filament with .1 A applied. Leads attached using silver epoxy.

We did not continue to conduct more rigorous testing for resistivity as a colleague corroborated the numbers and the resistivity was not far from the resistivity the manufacturers reported for the filament itself (before printing).

2.1.3 Initial Printing Parameters

Initially we printed with the default PLA parameters for the Electrifi conductive 1.75 mm filament. However, the key parameters we changed for the following initial tests were lowering the nozzle temperature to temperatures in the range 140-160 C, lowering the printing bed temperature to 30 C, and lowering the printing speed to 3000 mm/min. Later in the paper we make additional changes to optimize for printing and those final parameters can be seen in the appendix.

2.1.4 Conductive Filament Printer Accuracy Tests

In order to test the accuracy of the printer we printed some test structures with a pyramid step shape. Figure 2-1 below illustrates this shape in both the X and Y direction. The raw confocal microscope data in Fig. 2-1 is used to analyze printer accuracy (Fig. 2-2).

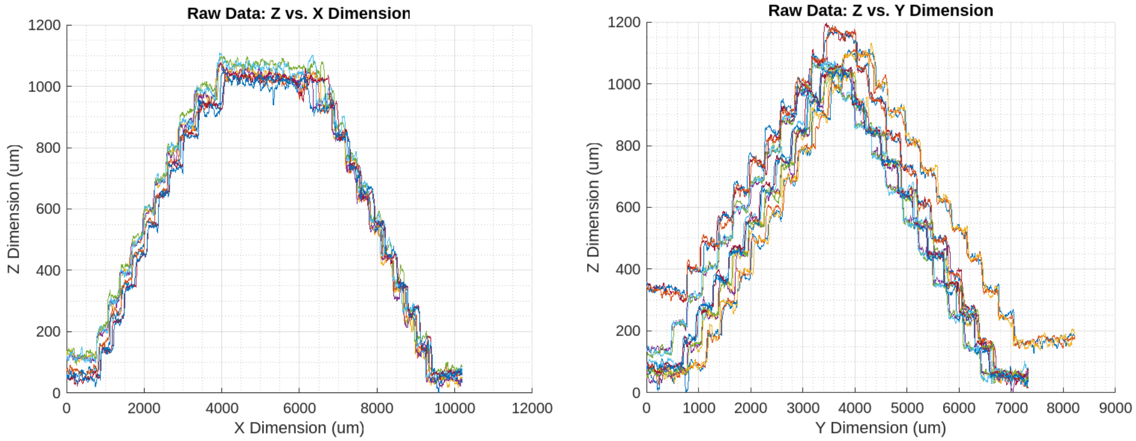

(a) X Dimension

(b) Y Dimension

Figure 2-1: Pyramid step structure measured in both the X and Y directions using a confocal microscope. X direction is 4 samples with two measurements for each and Y direction is 5 samples with 3 measurements for each.

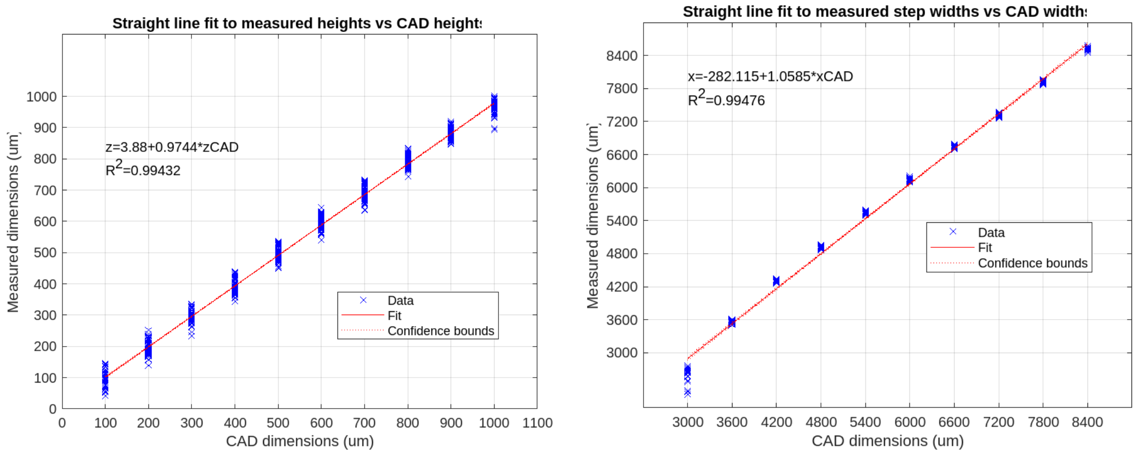

(a) X-Dim Height

(b) X-Dim Width

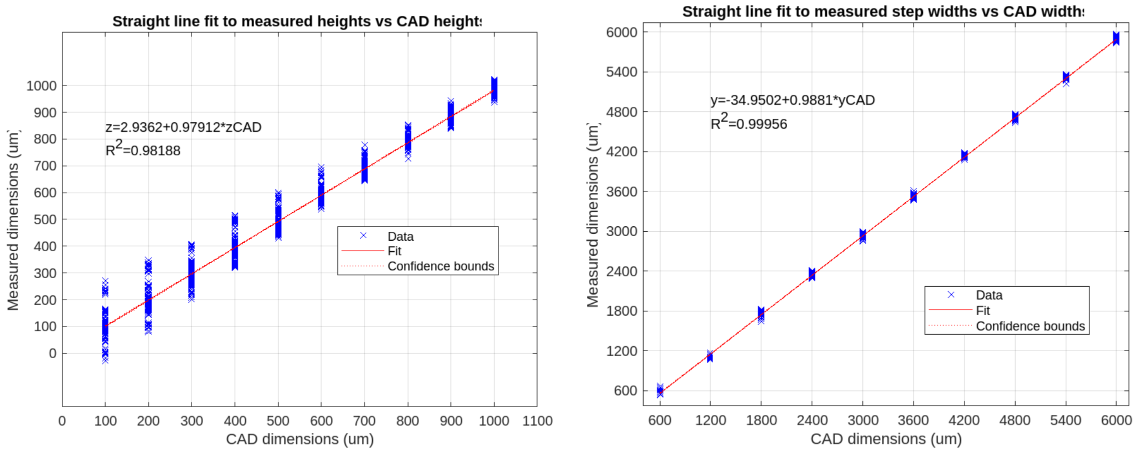

(c) Y-Dim Height

(d) Y-Dim Width

Figure 2-2: Distances between the steps (from the pyramid step structure in Fig. 2-1) with trend lines after being processed with a Matlab script.

The Matlab scripts for the above calculations and plots are included in the Appendix; the Matlab scripts were coded by a colleague, Jorge Canada. The X-dim and Y-dim widths visually have much less variation and much higher R^2 value. However, the CAD dimensions are also an order of magnitude higher, which explains this phenomenon. For the Y-dim. the average standard deviation for the XY direction is 30 microns and 25 microns for the Z direction. For the X-dim. the average standard deviation is 25 microns for the XY direction and 17 microns for the Z direction. However, the program did not account for the differences in slope between measurements, thus the accuracy is likely higher than measured.

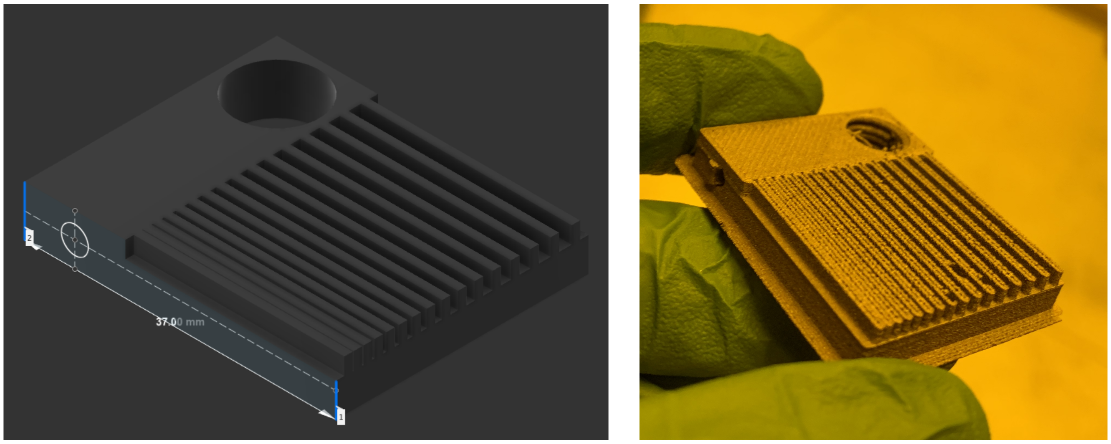

(a) CAD Design Height

(b) Printed Structure

Figure 2-3: Gap test structure 37 mm by 30 mm.

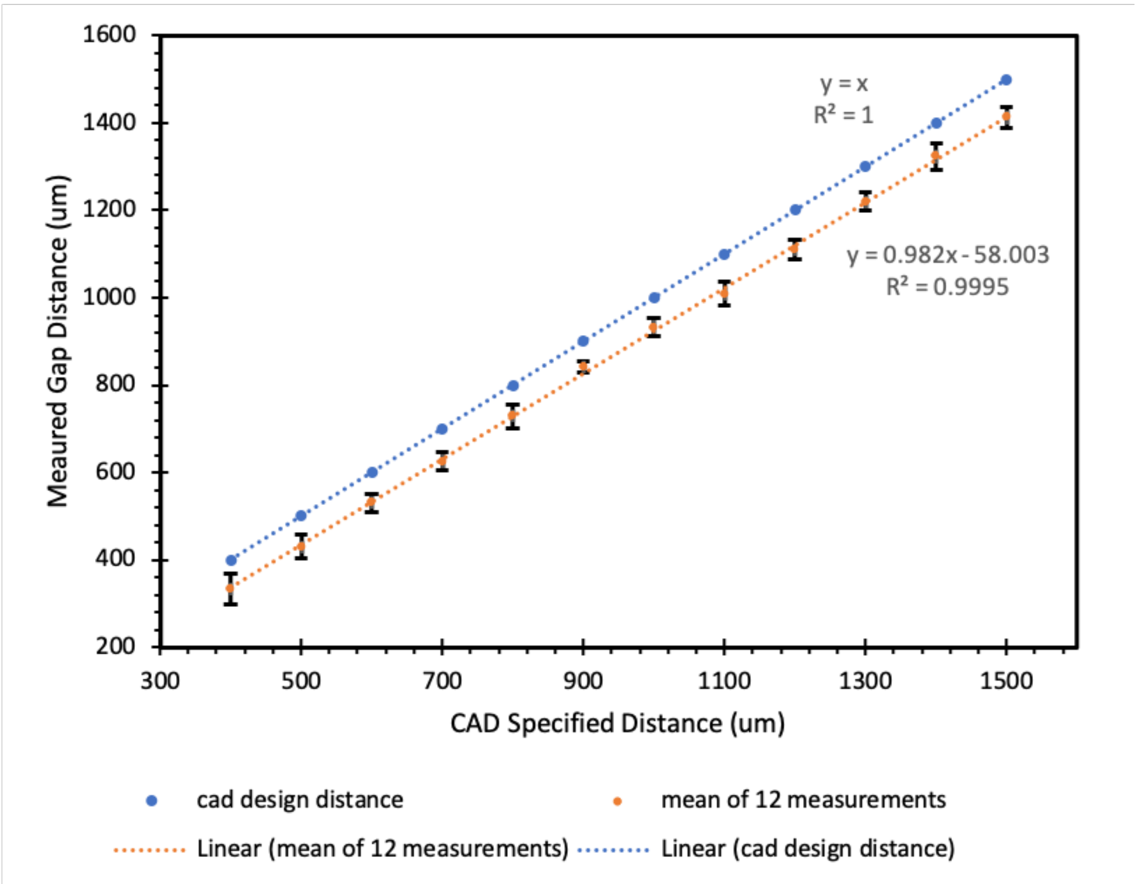

Figure 2-4: Gaps measured using test structure above (Fig. 2-3). All measurements done at 1900 micron height.

This additional test gave us an average standard deviation of 25.7 microns and an offset of about -58 microns from the CAD design. Note: Towards the end of the project we further optimized the printing and it is likely the accuracy is better than what we measured here initially.

Now that we have characterized the filaments, as well as the accuracy of printed structures with respect to the CAD files, we move on to monolithically printing quadrupole structures with our dual material extrusion process.

2.2 References

[2.1] Multi3D, *Multi3D Electrifi Conductive Filament*, Australian government, accessed 20 October 2022, `https://www.multi3dllc.com/product/electrifi/`

[2.2] Multi3D, *Electrifi FAQS*, Australian government, accessed 20 October 2022, `https://www.multi3dllc.com/faqs`

Chapter 3 Quadrupole Design and Fabrication

For the design of the mass filter we optimize between these characteristics of the quadrupole mass filter: mass range, resolution of the device, size, and power requirements. The following equations define the resolution of the device, key geometry parameters, and the amplitudes of the DC and RF signals applied to the quadrupole mass filter [3.1]. These equations are explained in depth in Ch. 1.

$$R = \frac{1}{h} * f^2 * L^2 * (\frac{m}{2 * v_z * e})$$

The resolution of the quadrupole grows quadratically with increasing length of the quadrupole, as well as the frequency driven across the quadrupole. This initially tells us that we should have as long a quadrupole as possible; however, there are limiting factors. Increased length has an increased printing failure rate and uses more material. Increased length also means that there is less transmission of ions and thus it is harder to measure the ions that pass through the quadrupole mass filter.

Knowing we had already settled on a frequency in the ∼1-3 MHz range, we settled on a ballpark figure of 10 cm quadrupoles (as this fits the constraints of a 6 L cube satellite and should achieve the desired resolution of 100) as a starting point. Initial tests were done with 7.5 cm quadrupoles to reduce printing failure opportunity and printing time.

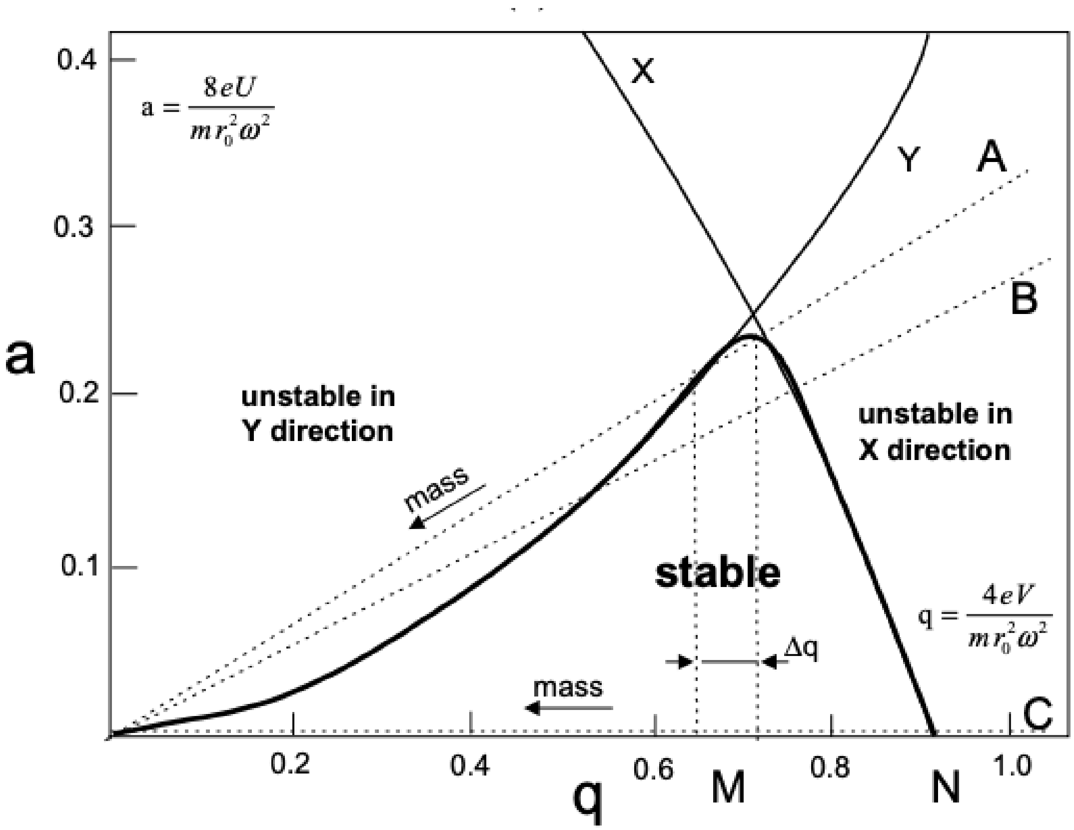

Figure 3-1: a and q parameter stable region for operation of mass filter [3.2].

$$a = \frac{8 * e * U}{m * r_0^2 * \omega^2}$$

$$q = \frac{4 * e * V}{m * r_0^2 * \omega^2}$$

Given the stability region above, defined by the equations and plot, we chose a and q to be .23 and .7, respectively. Then we solved for the DC and RF amplitudes required for our design. Given that e is assumed to be 1 and our frequency is ∼2 MHz we chose a diameter of 4 mm, which, at our maximum mass of 100 amu, required a 400 V_{pp} sinusoidal amplitude (which is near the voltage limit we desired). In this way we optimized for the best resolution given the constraints we imposed. Next we looked at the physical design of the quadrupole and the materials we would use.

3.1 Geometries and Design Requirements

Ideal conductive rods in a quadrupole mass filter have a hyperbolic shape and are separated by a diameter of radius r_0 [3.3]; therefore, we tested printing electrodes of this shape. We used an r_0 of 2 mm (which gives the 4 mm diameter we designed for).

Furthermore, while we know the ends of the rods should be hyperbolic, it is unclear how much of the rest of the rod should be conductive and how "thick" it should be, or rather how little conductive material we can use before suffering performance issues. In order to get a starting point for this we looked at the skin depth effects for the Electrifi filament. Skin depth is given by the following equation where p is resistivity $(\Omega * m)$, f is frequency (Hz), μ_r is relative permeability (assume to be 1), μ_0 is a permeability constant (assume to be $4 * \pi * 10^{-7}$).

$$\sigma_{electrifi} = \sqrt{\frac{p}{\pi * f * \mu_r * \mu_0}}$$

For Electrifi this gives a skin depth of 3.8 mm @2.65 MHz (for reference copper has a skin depth of.065 mm @2.65 MHz). In a layer 4x the skin depth from the surface of the conductor ∼98% of the current will flow in that layer. Therefore, we have an incentive to increase the Electrifi used because the width of our rods is in the range of ∼10 mm (<4x the skin depth). Thus, skin depth significantly affects the current and signals transferred.

There were further reasons not to minimize the volume/density of Electrifi printed. As the amplitude of the sinusoids increases across the quadrupole, we have increased current, which leads to increased heat dissipation in the Electrifi material. If we minimize Electrifi used, there is a lower heat dissipation rate and higher chance of failure. According to the manufacturer a 1x1 mm trace fails at 200 mA (fails means the resistance increases by 50%) [3.4]. Additionally while testing we had an instance where the quadrupole rods melted in the vacuum chamber and short circuited (due to inattentiveness and running the quadrupole at high voltages for an extended time). Therefore, thermal dissipation is important to consider and a factor that influenced the amount of Electrifi we printed with. With this in mind we go to initial designs, fabrication and troubleshooting.

3.2 Initial Fabrication and Troubleshooting

First we printed some trivial, small quadrupole structures to see if it was feasible to achieve monolithically printed, electrically isolated, conductive rods arranged in a circular pattern with a non-conductive filament housing. This caused us to arrive at the figure below.

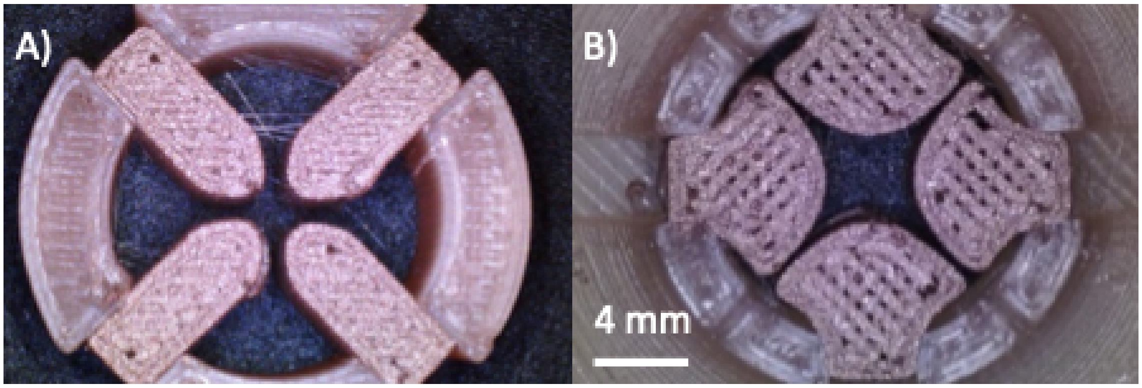

Figure 3-2: 3D Printed Quadrupoles— a) early version, b) later version with hyperbolic electrodes.

Once feasibility was determined the next step was creating test structures that we could actually use in the vacuum setup as quadrupoles.

3.2.1 Printing Problems

Fig. 3-3 contains an iteration of quadrupole printing that elucidates many of the problems that had to be overcome to properly print electrically isolated and conductive quadrupoles. Successive prints are numbered 1 to 5 from left to right.

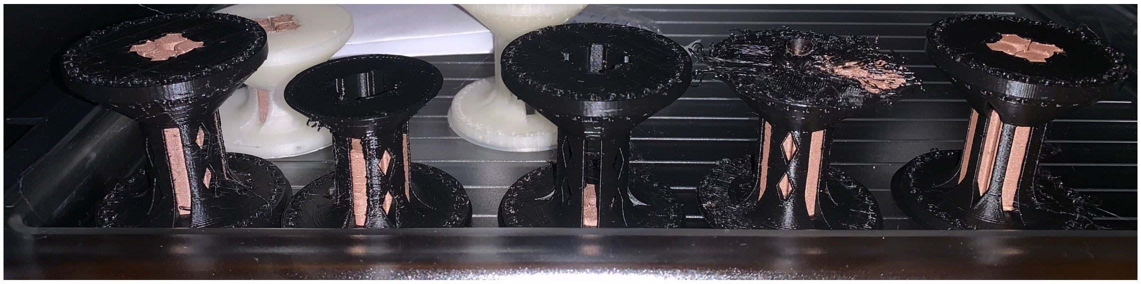

Figure 3-3: Quadrupole Printing Iterations. Diameter of the mounting plates of the quadrupoles shown is 5 cm.

1. The 1st print came out fully, but the conductive filament directly on the build plate was melting and not printing accurately. Also it was difficult to visually inspect conductive isolation of the rods (fixed in iteration 5 by exposing the entire length of the conductive rods where they might touch and short circuit).
2. The 2nd iteration did nott fully print and stopped early.
3. For the 3rd iteration the filament feeder was tightened. The bottom was deformed because of heat deformation and the print still failed partway.
4. For the 4th iteration the filament feeder was loosened and then the filament didn't strip, but the plate detached from the base.
5. For the 5th iteration the skirt outline is 7 lines instead of 4 (to get the quadrupole to stick to the build plate) and the quadrupole design is modified: instead of diamonds there is a long vertical exposed strip, r_0 is 2.11 mm instead of 2 mm, to hopefully resolve some of the conductive isolation issues, and the base of PLA at the bottom of the conductive rods is thicker (1.4 mm).

However, even the 5th iteration in Fig. 3-3 suffered from non-electrically isolated conductive rods, despite the larger r_0 and shortly thereafter there were continued issues with prints failing midway. Not to mention that the desired quadrupoles for testing would ideally be longer, in the range of 7.5 to 12.5 cm, rather than 5 cm like the quadrupoles in Fig. 3-3 (this would likely introduce more printing errors given the increased printing time longer quadrupoles require).

The filament continued to strip in subsequent prints and a couple of nozzles also became clogged, which either required using cleaning filament or in some cases replacing the entire nozzle. The filament feeder was stripping the filament no matter how loose or tightened it was. For a colleague who had short prints this stripping was not an issue as it usually only happened a couple hours or more into a print. Many sources of error (enumerated below) were considered before arriving at a solution.

1. High humidity causes the filament to contain high levels of water and extrude improperly.
2. Nozzle temperature may be affecting extrusion.
3. Heat creep from the nozzle up to the filament feeder softens the filament and causes it to strip.
4. Filament retraction increases the chance of stripping.
5. Heat from the enclosure softens the filament and causes it to strip.

All of these possible failure/adjustment possibilities had some validity to them and also many depended on each other, so it was difficult to systematically target and eliminate each of the problems. Solutions attempted: changing the nozzle temperature; adding fans to decrease heat creep and filament temperature; decreasing the filament retraction; and changing bed temperature.

Eventually, after going through many of these parameters (sometimes in tandem) and as prints continued to fail midway, in order to allow the maximum heat to escape, the printing enclosure was left open for the duration of the print job. This solved the issue! It seems that despite the fans dispersal of heat, the combination of heat creep from the nozzle temperature, bed temperature, and enclosed space still proved to raise the temperature too high for the filament. This caused the filament feeder to strip the softened conductive filament.

With this solved, the next step was printing longer quadrupoles.

3.2.2 Printing Profiles

The final printing profiles for the quadrupoles are included in the Appendix. The conductive filament parameters were much more heavily iterated than the non-conductive parameters; however, the parameters of both are included.

Important Note: in order to print at the low temperatures that the conductive filament required we contacted MakerGear—they suggested including the line "M302 P1" within the Slicer's starting script to print at temperatures under 170°C. This is necessary because the Makergear printer has a safety function installed that restricts extrusion/retraction when attempting to extrude while under 170°C.

3.3 Full Size Quadrupoles

The next step was printing longer quadrupoles that could be vacuum tested. As you can see in Fig. 3-4, the quadrupoles have a base and top plate that have many mounting holes of different diameter that allow for easy attachment to our setup in vacuum (four 12.5 cm M1.6 threaded rods run through these mounting holes on the quadrupole and hold the quadrupole in place with small nuts).

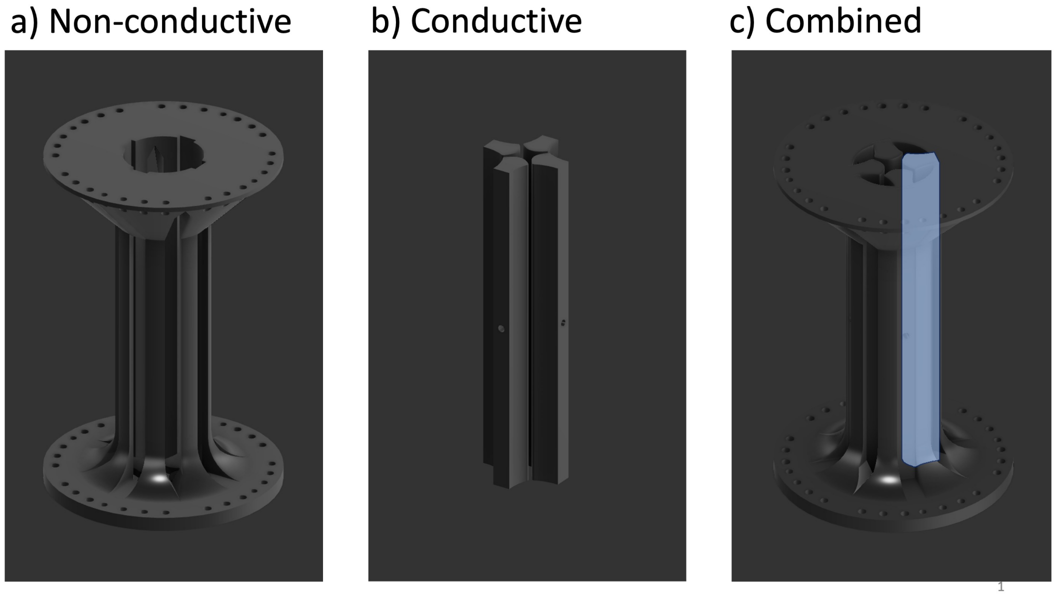

Figure 3-4: CAD Design for 7.5 cm Quadrupoles: a) Non-conductive housing. b) hyperbolic, conductive, electrically isolated rods with 4 mm diameter. c) combined conductive/non-conductive with a hyperbolic rod highlighted.

Fig. 4-1 in the next chapter displays these quadrupole designs printed with attached leads (using the printing profiles in the Appendix).

3.4 Experimenting w/ Metal Plating

Additionally, experimentation with the plating of the PLA and conductive filament was conducted (room-temperature metallization of electroless copper and nickel plating). The procedures for both plating methods are contained in the Appendix (procedure created by a colleague, Nicholas K Lubinsky).

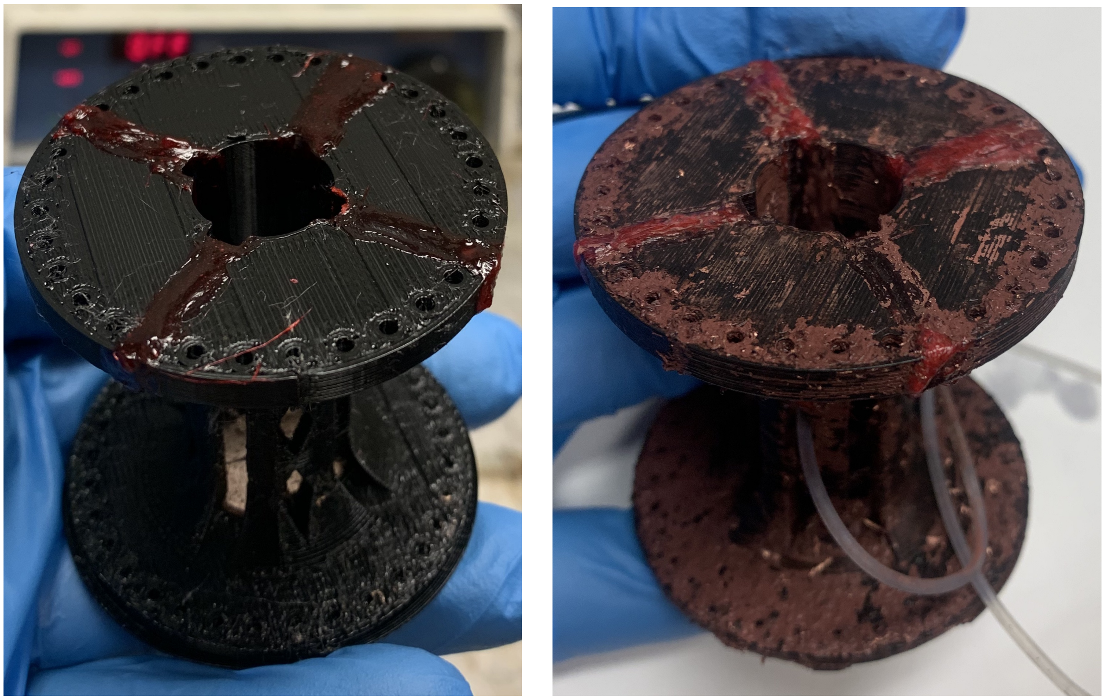

(a) PLA with masking paint.

(b) PLA after copper plating.

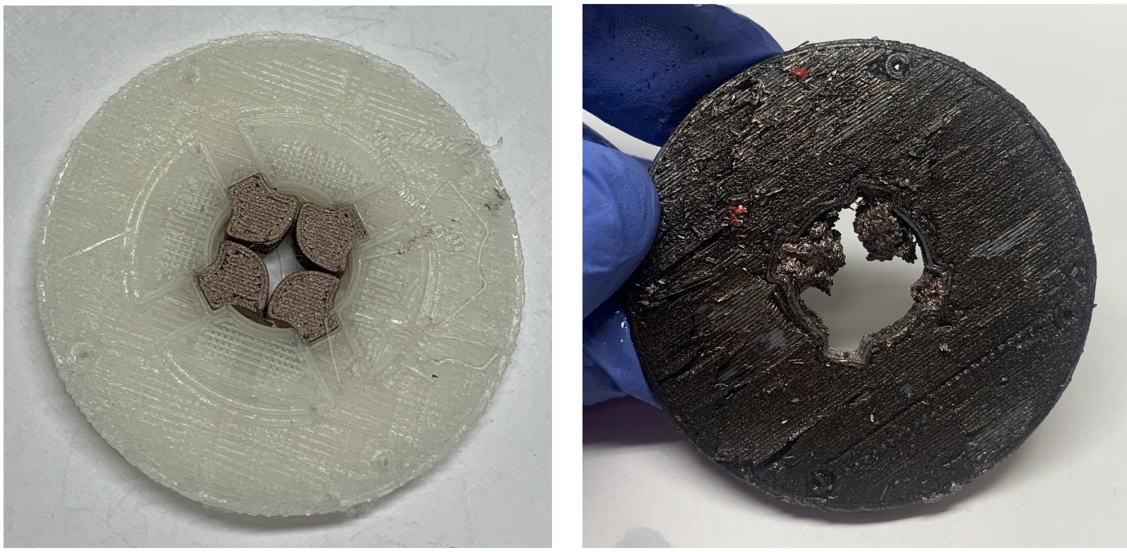

(c) PLA w/ Conductive Filament

(d) PLA w/ Conductive Filament w/ Nickel Plating

Figure 3-5: Plating for copper @ 35 C for 90 minutes and plating for nickel @ 65 C for 70 minutes. Diameter of the circles shown is 5 cm.

Both the copper and nickel plating yielded promising results. Copper plating unfortunately did not deposit well on the PLA surface and did not allow for reliable conductivity. However, copper did plate on the Electrifi filament—perhaps a quadrupole with Electrifi rods could be plated with copper in order to achieve lower resistance, better heat dissipation performance, better geometry, higher resolution, etc. Future work could include copper plating of Electrifi for better quadrupole performance.

Nickel plating is conducted at a higher temp of 65 C (achieved by adding dimethylamine borane as directed in the appendix) and at this temperature the Electrifi melts away and deforms. However, the regular PLA did plate and the conductivity performance was promising. Future work could include nickel plating of PLA or other extrusion compatible materials with extrusion temps 100 C+ (such as PEEK). In this scenario, conductive filament would not be required—the entire structure would be printed out of a single material. Then the structure would be painted with masking paint to isolate the quadrupole rods and finally plated with nickel.

3.5 References

[3.1] Cheung, K. "Chip-Scale Quadrupole Mass Filters for a Micro-Gas Analyzer", 2009.

[3.2] Wilamowski, B., et al., IECON'01. 27th Annual Conference of the IEEE Industrial Electronics Society (Cat. No.37243), "Enhancing The Sensitivity of Miniaturized Quadrupole Mass Spectrometers", DOI: 10.1109/iecon.2001.976470

[3.3] D. J. Gershman, B. P. Block, M. Rubin, M. Benna, P. R. Mahaffy, and T. H. Zurbuchen. Higher order parametric excitation modes for spaceborne quadrupole mass spectrometers. Rev. Sci. Instrum. 82, 125109 (2011). DOI: 10.1063/1.3669781

[3.4] Multi3D, *Electrifi FAQS*, Australian government, accessed 20 October 2022 `https://www.multi3dllc.com/faqs/`

Chapter 4 Quadrupole Testing & Data

First we will review the performance of the monolithically printed quadrupoles as collision cells and then we will discuss their performance as quadrupole mass filters. All tests conducted in this chapter are with an Ardara Filament Power Supply [4.1], Optics Power Supply [4.2], and Quadrupole Power Supply [4.3].

4.1 Quadrupole as an RF Guide

Fig. 4-1 shows multiple, monolithically 3D-printed, RF quadrupoles. These were printed using the processes described in Ch. 3. Conductive epoxy was used to connect the yellow leads to the opposing sides of the quadrupole. 22 AWG was used for these short leads, which are fed to shielded coaxial cables that connect to the exterior of the vacuum chamber.

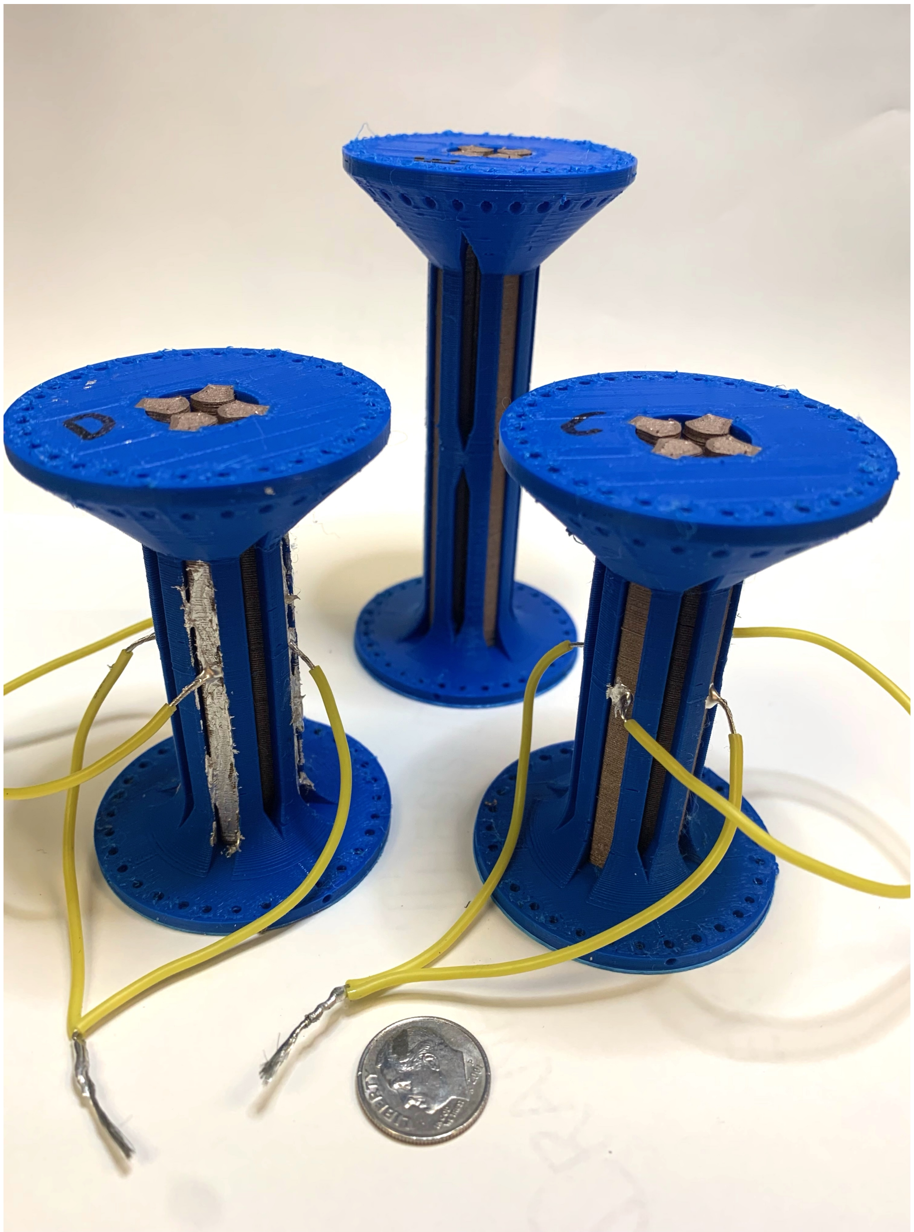

Figure 4-1: Monolithically 3D-printed, compact quadrupole collision cells next to a US dime coin. Silver, conductive epoxy is used to attach leads to the conductive rods.

Fig. 4-2 shows a 7.5 cm collision cell from Fig. 4-1 integrated into a commercial electron impact gas ionizer. A Faraday plate measures the current on the opposite end. (There is a Faraday cage around the Faraday plate because we were initially receiving significant radiation from the sinusoidal waves across the quadrupole). These pictures are before installation into a vacuum chamber (base pressure 4 x 10^{-8} torr).

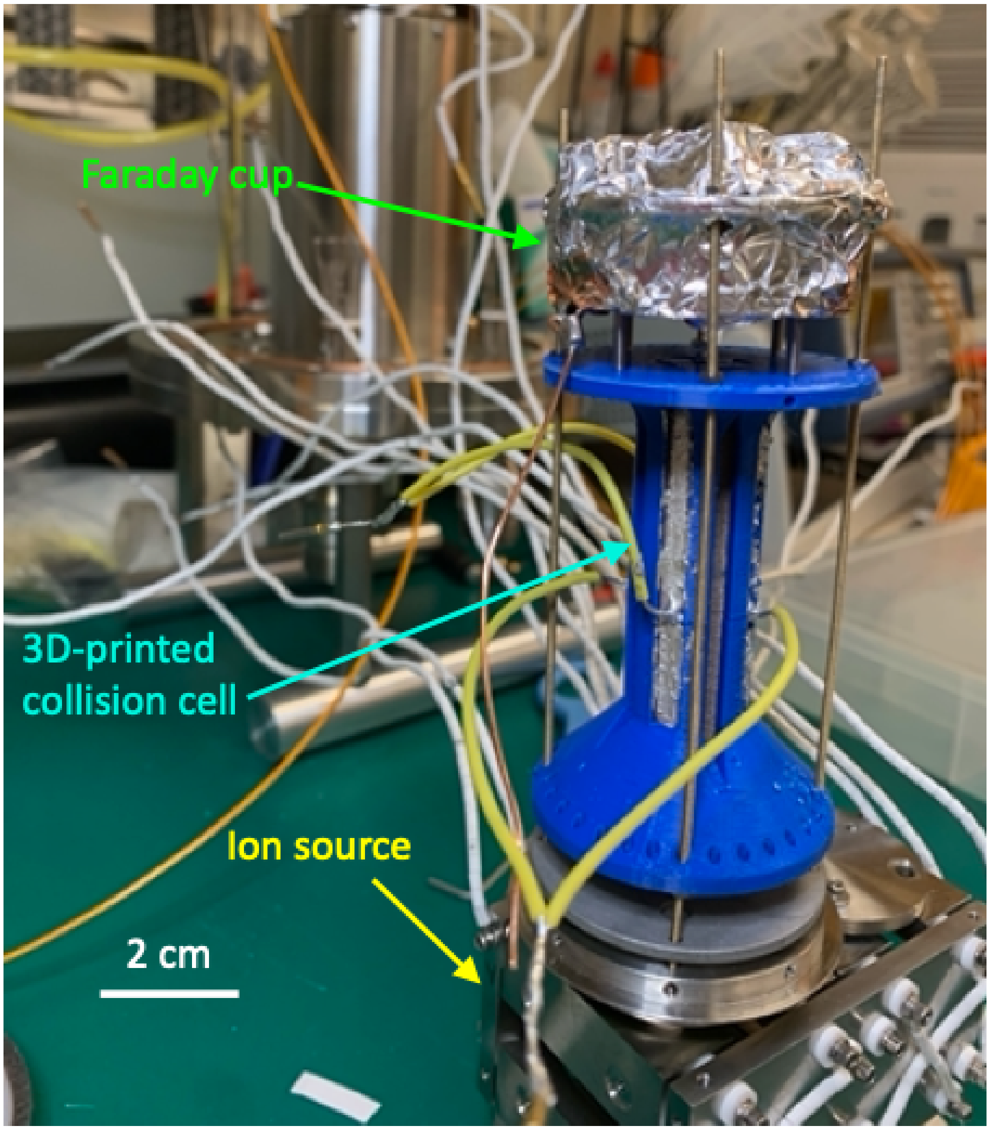

Figure 4-2: A 3D-printed quadrupole collision cell integrated with an ionizer at the bottom and a Faraday plate within a Faraday cage at the top.

The RF quadrupole guide has a capacitance of 13.88 pF and a resistance of 288 ohms when measuring with an LCR meter at 1 MHz and 1 V amplitude. However, the capacitance once the quadrupole was in the chamber was 12.4 pF. The tests were run using a script (included in the git repository linked in the Appendix) that commands the two Keithley Power Supplies in the lab. This script varies a command voltage to our Ardara Quadrupole Power Supply [4.3] that varies the amplitude of the sinusoidal waves. The 2nd Keithley collects current from the Faraday plate simultaneously. In this way we are able to vary the amplitude of the sinusoidal waves and collect current at the same time.

The parameters that were tuned were the ion optics voltages that focus the ions (pertaining to the Ardara equipment). We also had to choose the parameters for the thermionic ionizer. These are shown below.

Pole Bias	Extractor Lens	Deflector Inner	Deflector Outer	Deflector Entrance	Quad Entrance	Quad Exit
0 V	-10 V	-350 V	-35 V	-130 V	-20 V	-120V

Table 4.1: Voltages applied to Ardara lenses and focusing structures in the vacuum chamber.

Focus Lens	Def. B Outer	Def. B Inner	Def. Top/Bot Plates	Deflector Exit	Pre-Filters
10 V	-40 V	-350 V	-20 V	-100 V	-10 V

Table 4.2: Voltages applied to Ardara lenses and focusing structures in the vacuum chamber.

Ion Region	Electron Energy	Emission Current
7 eV	-80 eV	.4mA

Table 4.3: Parameters for the thermionic ionizer.

With the parameters defined and the script for driving voltages and measurements, we go on to testing of the quadrupole as a collision cell for possible use in a triple quadrupole mass spectrometer [4.4].

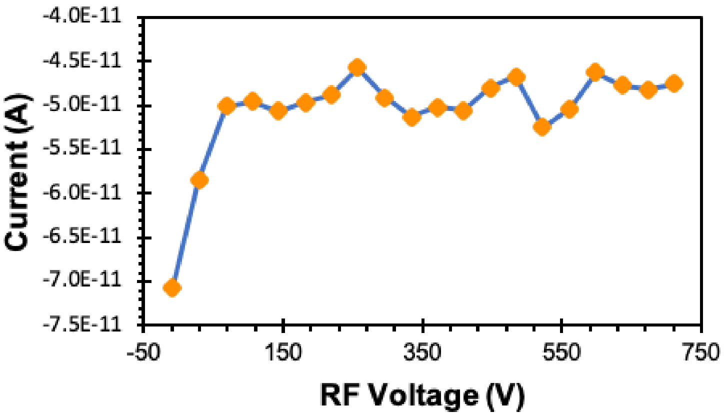

(a) ionizer off (baseline)

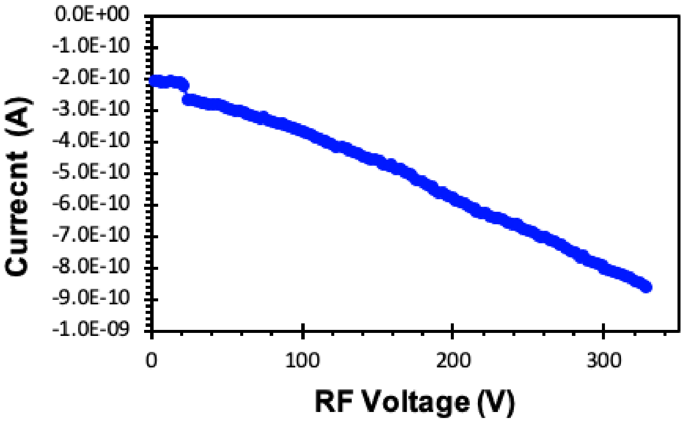

(b) ionizer on

Figure 4-3: Measured ion current vs. RF V_{pp} amplitude applied across the collision cell. Base pressure 4×10^{-8} torr. Argon introduced (4 x 10^{-4} torr). a) Collector plate baseline current measurement; ionizer off; RF voltage on the quadrupole collision cell (2.680 MHz); b) ionizer on.

Fig. 4-3 a) shows a noise floor centered at 50 pA. With the quadrupole off, ionizer on, ion transmission is 2 pA (not pictured), which is hardly distinguishable from the noise floor; however, if the quadrupole is powered with the RF sinusoidal signal and the ionizer is on, there is a 2-3 orders of magnitude increase in ion transmission as the RF amplitude increases linearly (Fig. 4-3 b)). This shows that the quadrupole can perform and channel ions. Therefore, this quadrupole could be used as a collision cell in a triple mass spectrometer. However, the main objective is to characterize the quadrupole as a mass filter (discussed in the following section).

4.2 Quadrupole as a Mass Filter

To test the quadrupole as a mass filter the same sinusoidal amplitudes are applied, but with symmetric and opposite DC amplitudes.

4.2.1 Quadrupole Setup

Below we show the setup we used in vacuum to hold the quadrupole in place and generate the ions necessary to test the quadrupole. We used the same 7.5 cm quadrupole that we tested as a collision cell above. However, this time we used an Einzel lens to focus the ions and used the Ardara built-in Faraday plate instead of our own Faraday plate with a Faraday cage.

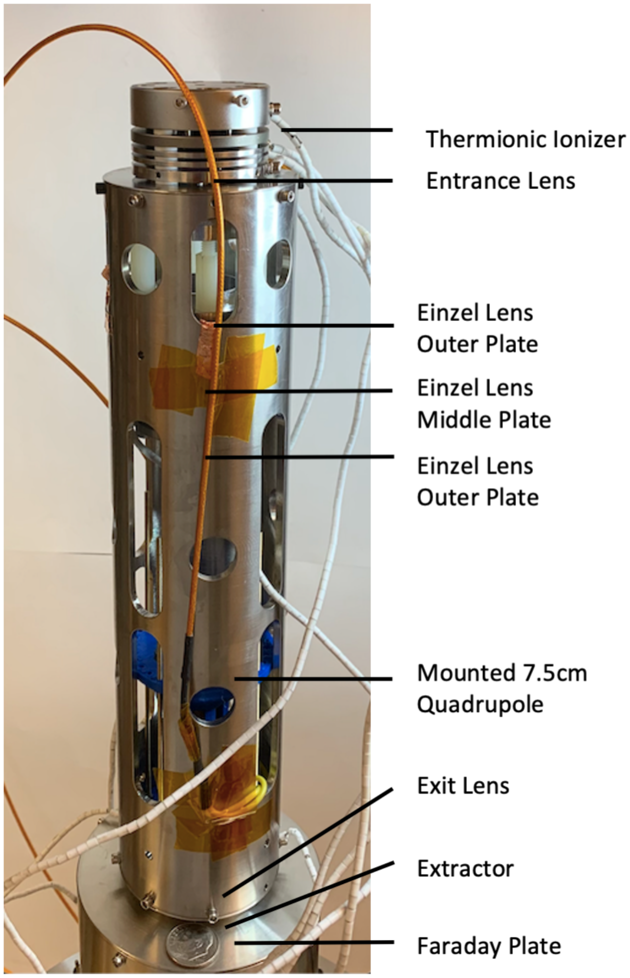

Figure 4-4: Quadrupole Vacuum Setup w/ an Einzel lens and Faraday cup. We use a thermionic ionizer to ionize the gas that is in the chamber. US Dime coin included.

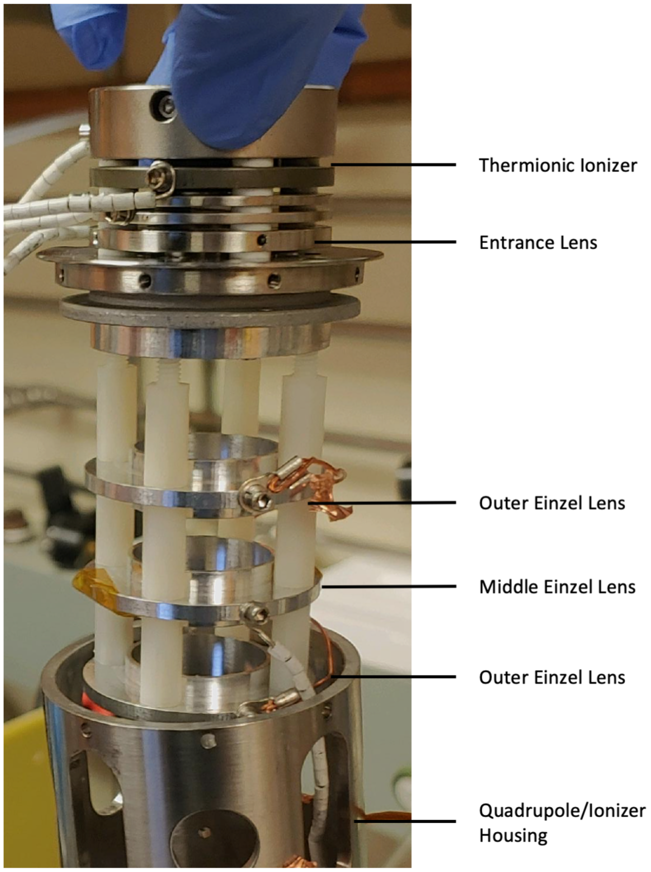

Figure 4-5: Einzel lens. Inner diameter of the metal housing is 5 cm.

Einzel lens voltages, other lens voltages and ion parameters are below. Different from the previous testing of the quadrupole as a collision cell, this time the bulky rectangular prism was removed (containing additional Ardara ion optics). This reduced the number of variables/parameters we had. Instead the ions were sent into our custom Einzel lens directly (to focus the ions into the quadrupole). The parameters used are below.

Extractor Lens	Einzel Outer Lenses	Einzel Inner Lens	Quad Exit	Quad Entrance
-2.4 V	0 V	-40 V	-65 V	-20 V

Table 4.4: Voltages applied to Ardara lenses and focusing structures in the vacuum chamber.

*P*ole Bias	Delta Res	Delta M
0 V	5	5

Table 4.5: "Pole bias" biases both sinusoidal waves with the DC value and Delta Res and Delta M control the ratio of RF to DC amplitude in the sinusoidal waves.

*I*on Region	Electron Energy	Emission Current
9.8 eV	-70 eV	.415 mA

Table 4.6: Parameters for the thermionic ionizer.

4.2.2 7.5cm Quadrupole Testing

Once we were ready to begin tests, the script that commands the two Keithley power supplies was used (same script as discussed above). The Faraday plate was biased at 0 V.

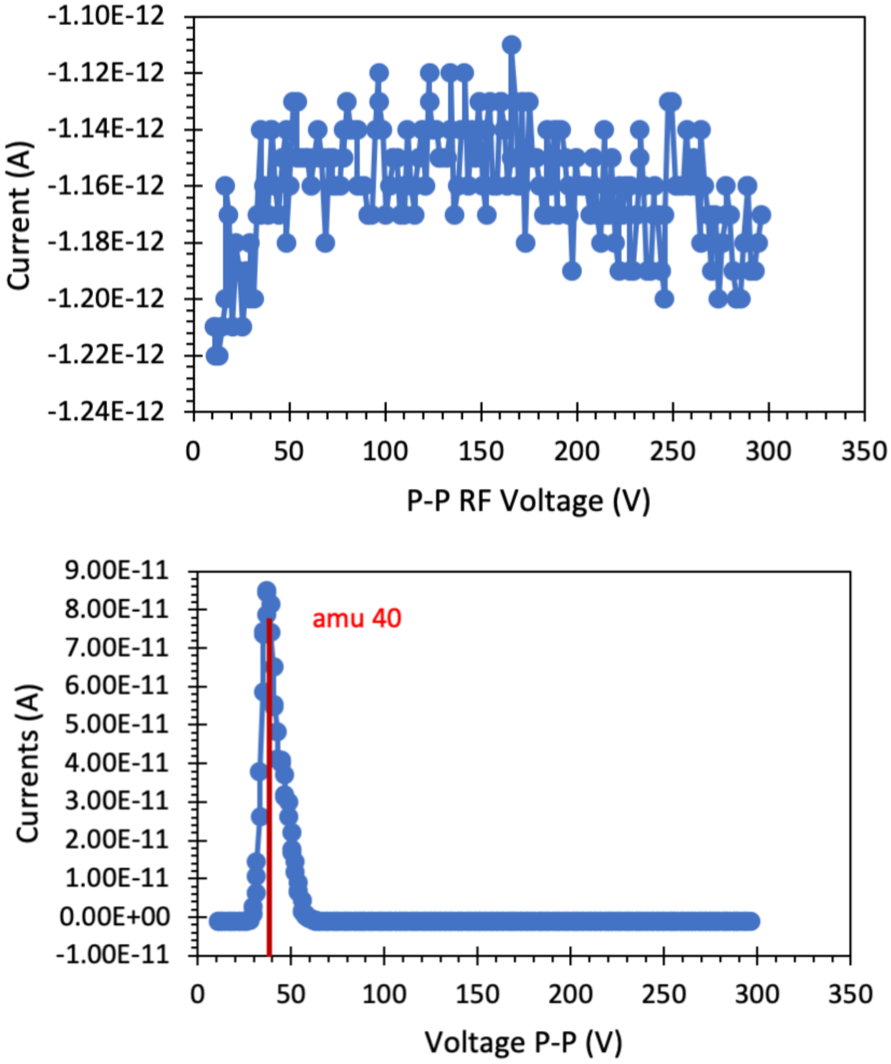

Figure 4-6: Collector current vs. P-P RF bias voltage with a) ionizer off (baseline), b) ionizer on. Red line indicates expected peak of amu 40 according to the Mathieu equations. In both cases the background is Ar @ 4×10^{-4} torr.

The first graph shows a baseline centered around -1.15 x 10^{-12} A. The second graph, with the ionizer on, clearly shows a peak at ~39 V_{pp} that is orders of magnitude above the baseline noise. The theory, using the equations defined earlier expects the peak to be around 38.3 V_{pp}, which corresponds to the peak in the graph. It is clear there is only one peak in this second graph which is what we expect since we only have Argon in the chamber. The resolution can be obtained from the graph.

Earlier we defined resolution as:

$$R = \frac{1}{h} \ * f^2 * L^2 * (\frac{m}{2 * v_z * e})$$

The resolution is a function of h (a constant determined by a and q—for 1st stability region $h = 15$), L (quadrupole length in cm), f (frequency in MHz), m (amu), v_z (axial ion velocity), and e (assumed to be 1) [4.5]. Using this equation we arrive at a max resolution of ∼180 for argon mass 40. To find the actual resolution achieved, we use the following equation to extract resolution from the mass spectra graph.

$$R = \frac{m}{\Delta m}$$

Δm is measured at half the peak height (full-width half maximum—FWHM) which gives a delta of 8 volts between 34 V and 42 V or ∼8 amu; the measured mass is 40 amu so the resolution is $40/8 = 5$ for the previous experiment. This resolution is much lower than the expected resolution of 180. We believe this is due to non-linearities in the geometry of the quadrupole, electrode alignment, and the conductivity/heat dissipation properties of the Electrifi filament. For reference, other similar compact mass spectrometers can have resolution 1-2 orders of magnitude higher [4.6], which means while this shows promise, more work has to be done to increase resolution achieved.

Thus we have shown functionality of our 3D-printed, monolithic quadrupole as both a collision cell and as a quadrupole mass filter. We also tested the quadrupoles at higher frequencies and with the compound FC-43.

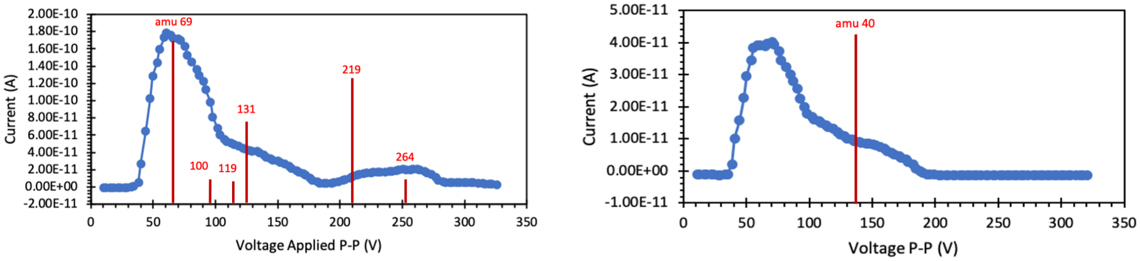

(a) @1.34MHz FC-43 1.9x10-4 torr

(b) @2.53MHz Argon @ 8.6×10-4 torr

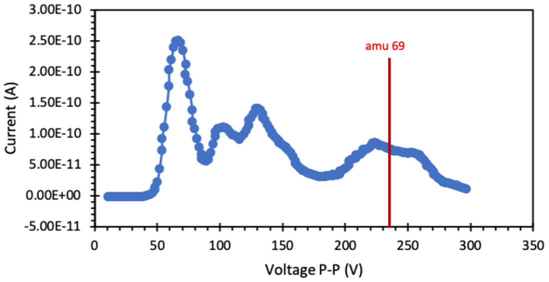

(c) @2.53MHz Argon 1.25x10-4 torr

Figure 4-7: Collector current versus RF voltage P-P tests. Red line indicates expected peaks for either Argon or FC-43 according to the Mathieu equations. Base pressure 1.27 x 10^{-8} torr. All ion optics and associated parameters are the same (Table 4.4, 4.5, 4.6) except c) extractor @ -16.4 V; Einzel inner lens @ -34.4 V

At this point the data becomes more unclear. We believe there are non-linearities in the geometry of the quadrupoles, as well as heat dissipation issues that contribute to data that does not reflect the theory.

For graph a) in Fig. 4-7 the first peak of FC-43 at 1.34 MHz lines up with the theory (empirical resolution of ∼1.5 based on graph), but the following peaks of higher masses are difficult to discern and it is clear the quadrupole is not clearly resolving these masses.

For graph b) in Fig. 4-7 the expected peak location does not line up with the actual peak for argon (empirical resolution of ∼1.5 based on graph).

For graph c) in Fig. 4-7 the expected peak locations should be at much higher RF amplitudes. However, if we put the theory aside for a second, the peaks do closely resemble the mass spectrum for FC-43 shown below (Fig. 4-8). The first 3 peaks would be mass 69, then 110 and then 131. The last peak would be mass 219. This seems reasonable given the close resemblance; however we cannot directly explain the deviation from the theory. The empirical resolution for the first peak is ∼3.5.

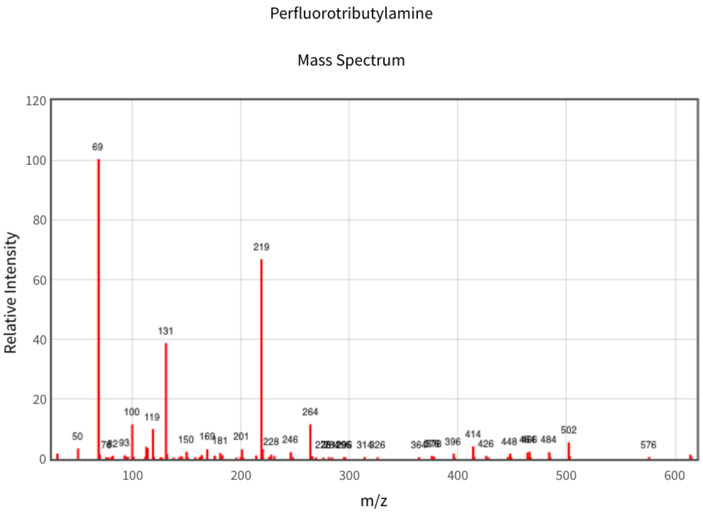

Figure 4-8: Mass Spectrum for the FC-43 compound used to test the quadrupole [4.7].

4.2.3 10cm Quadrupole Testing

The following testing is done with a 10 cm quadrupole, which has little changed to the physical structure except the quadrupole is elongated by an extra 2.5 cm. The quadrupole has a capacitance of 18.85 pF and resistance of 240 ohms in the vacuum chamber when measuring using an LCR meter at 1 MHz and 1 V amplitude. Based on the theory we expect a ∼2x increase in resolution from the increased length alone and also expect the peaks to shift up and require higher RF and DC voltages (because the frequency is higher for these tests—2.53 MHz).

The setup we use for the 10 cm quadrupole is fundamentally different. There is no Einzel lens. Instead we decrease the length of the housing surrounding the quadrupole and expect the proximity of the ion outlet to the entrance of the quadrupole to provide sufficient ions.

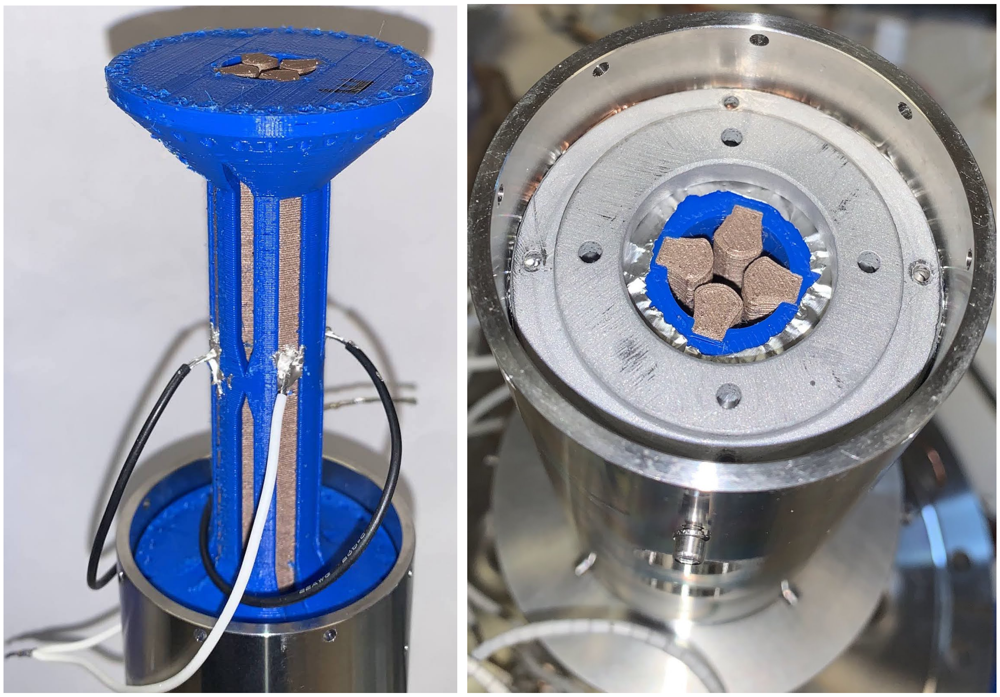

Figure 4-9: Left: 10 cm quadrupole w/ leads attached. Right: Top view of 10 cm quadrupole in metal housing with a top plate biased to ground (Inner diameter of metal housing is 5 cm)

Figure 4-10: 10 cm quadrupole in metal housing with ionizer on the top and Faraday plate below. US dime coin for reference.

*P*ole Bias	Delta Res	Delta M	Extractor Lens	Quad Exit	Quad Entrance
0 V	5	5	-10 V	-79 V	-20 V

Table 4.7: "Pole bias" biases both sinusoidal waves with the DC value and Delta Res and Delta M control the ratio of RF to DC amplitude in the sinusoidal waves. The last two voltages are applied to Ardara lenses that focus the ions.

*I*on Region	Electron Energy	Emission Current
9.8 eV	-70 eV	.3mA

Table 4.8: Parameters for the thermionic ionizer.

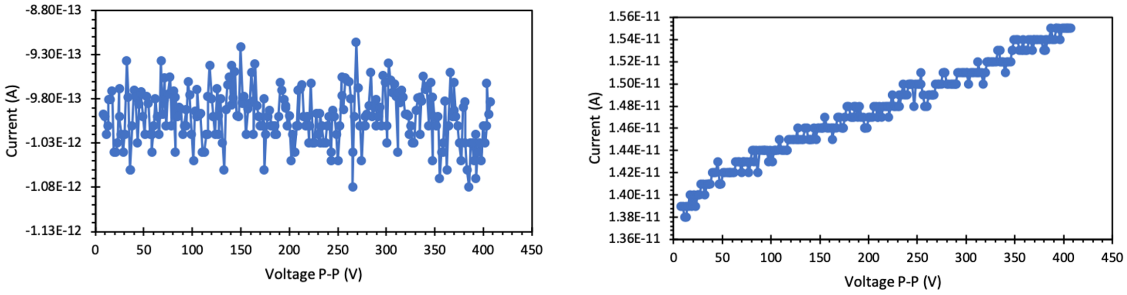

(a) Baseline Ar 2.2 x 10^{-4} torr. Just RF/DC

(b) Baseline Ar 2.2 x 10^{-4} torr. Just Ions

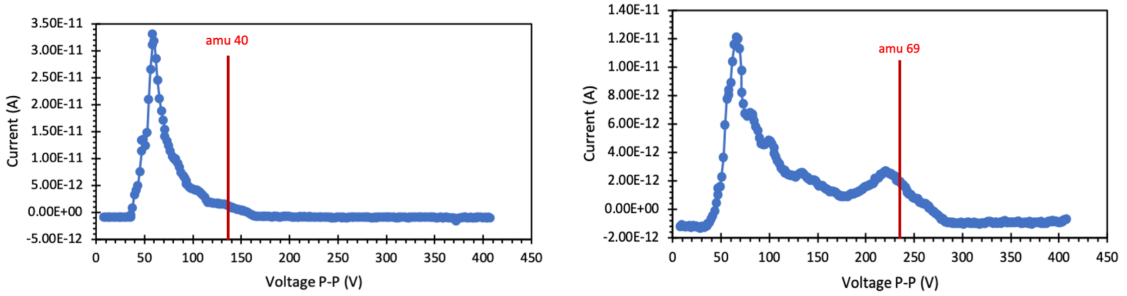

(c) @2.53MHz Ar 2.2 x 10^{-4} torr

(d) @2.53MHz FC-43 1.3 x 10^{-4} torr

Figure 4-11: All tests @2.53MHz. 2.1 x 10^{-7} torr baseline pressure. a) and b) are just baseline tests with either just the quadrupole being powered with the RF+DC or just the ion source on. Baseline in a) is very low and opposite sign. Baseline in b) is ∼15 pA without filtering and is slowly increasing as the thermionic ionizer warms up.

For both graphs we do not get peaks where we would expect for 2.53 MHz; however, as before, the results do seem to show just a single peak for Argon and multiple peaks for FC-43 as we would expect. Graph a) in Fig. 4-11 has an empirical resolution of ∼3.5). Graph b) in Fig. 4-11 has an empirical resolution of ∼3.5 for the first peak.

4.3 References

[4.1] Ardara, *Filament Power Supply*, accessed January 2023, `https://www.ardaratech.com/products/electronics/filament-power-supply`

[4.2] Ardara, *Optics Power Supply*, accessed January 2023, `https://www.ardaratech.com/products/electronics/optics-power-supply`

[4.3] Ardara, *Quadrupole Power Supply*, accessed January 2023, `https://www.ardaratech.com/products/electronics/quadrupole-power-supply`

[4.4] Yost R. A. (2022). The triple quadrupole: Innovation, serendipity and persistence. Journal of mass spectrometry and advances in the clinical lab, 24, 90–99. DOI: 10.1016/j.jmsacl.2022.05.001

[4.5] Cheung, K. "Chip-Scale Quadrupole Mass Filters for a Micro-Gas Analyzer", 2009.

[4.6] Syms, R. R. A., & Wright, S. (2016). MEMS mass spectrometers: the next wave of miniaturization. Journal of Micromechanics and Microengineering, 26(2), 023001. DOI: 10.1088/0960-1317/26/2/023001

[4.7] National Institute of Standards and Technology, *Perfluorotributylamine*, accessed January 2023, `https://webbook.nist.gov/cgi/cbook.cgi?ID=C311897&Units=SI&Mask=200`.

Chapter 5 Driving Electronics Design and Circuitry

Our work includes developing compact, low-power, precision electronics for driving the quadrupole. The requirements for the function of a quadrupole mass filter are two 180 degree out-of-phase, RF sinusoidal waves at specific frequencies and amplitudes with DC offsets [5.1]. These DC offsets for both sinusoidal waves are symmetric about 0V and opposite. The value of the DC offsets are related to the amplitude of the RF sinusoidal waves as a function of the defined parameters a and q given by the equations below [5.1].

$$a = \frac{8 * e * U}{m * r_0^2 * \omega^2}$$

$$q = \frac{4 * e * V}{m * r_0^2 * \omega^2}$$

Our design of a compact 3D-printed RF quadrupole mass filter is intended for chemical analysis of the ionosphere (1 to 100 Da range) that operates in the MHz range (<1 amu peak width across 1-100 amu, i.e., 100:1 resolution). The resolution is a function of h (a constant determined by a and q—for the 1st stability region $h = 15$), L (quadrupole length in cm), f (frequency in MHz), m (amu), v_z (axial ion velocity), and e (assumed to be 1) [5.1].

$$R = \frac{1}{h} * f^2 * L^2 * (\frac{m}{2 * v_z * e})$$

In order to accomplish this amu range and resolution, we arrived at creating 4-400

V_{pp} sinusoids with 0.2 V voltage steps (about 2000 steps), 10 cm length and 4 mm radius between the rods of the mass filter, w/ 0.33 to 33 V DC voltage offsets. These values are a ballpark to center the work on circuitry and geometries.

5.1 Driving Electronics Design

Our goal was to maximize power efficiency and thus we looked at several different amplifier topologies. Of the standard amplifier topologies the Class D topology offers the highest efficiency along with the lowest distortion of the signal [5.2]. It was also important that we use a full-bridge configuration (vs. half-bridge configuration) to achieve higher output power and efficiency despite the added complexity of a full bridge design.

In this way we decided on a Full Bridge Class D amplifier for the 1-3 MHz range (our design was made to have the capability of changing the frequency, which allows for added flexibility). The Class D Amplifier then feeds a transformer network and then two series tunable RLC resonant circuits. We then took this design idea and simulated the most design critical components in LTSpice to see feasibility etc.

However, as a side note: initially we had difficulty implementing the Class D, full-bridge design, so we looked into other options to generate the sinusoidal waves without a half-bridge (and therefore, less complex electronics, but unfortunately also using more power). This approach is conceptually more simple and fully outlined in the Appendix. We used the Buffer Board from Fig. 5-6 to directly drive the transformer network, with a variable resistor in series—in order to control the current driven across the transformer and thus control the amplitude of the sinusoidal wave. The circuit was quickly modeled in Falstad and also tested with a PCB. The circuitry and approach is described in the Appendix; however, the rest of this chapter will focus on the Class D full-bridge design because of the higher performance qualities.

5.1.1 LTSpice Simulation

The LTC7060 chip was used to control the PWM signals for the 4 driving MOSFETs as it only requires a single PWM input (which a microcontroller can easily supply). The full-bridge then feeds two parallel transformers that drive the two RLC circuits and quadrupole with the sinusoidal waves.

The DC voltage applied to the "top" of the full bridge controls the amplitude of the sinusoidal waves across the quadrupole (the quadrupole is modeled by two capacitors tied to ground).

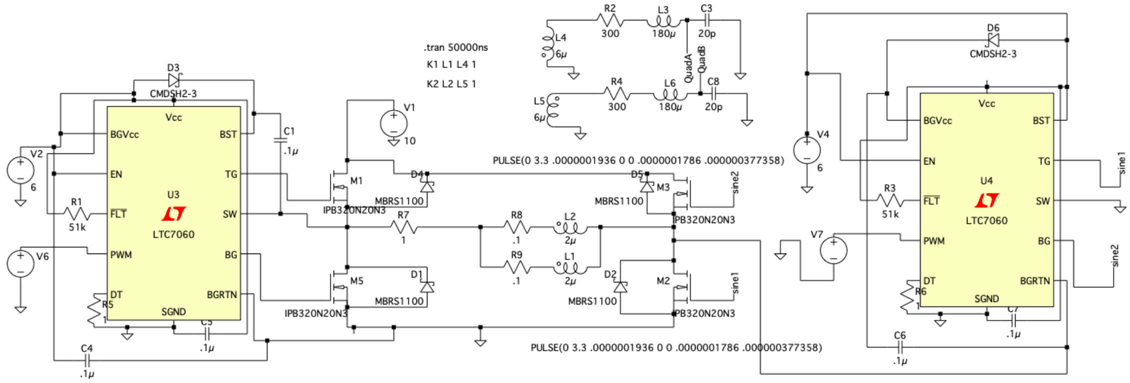

Figure 5-1: LTSpice simulation schematic.

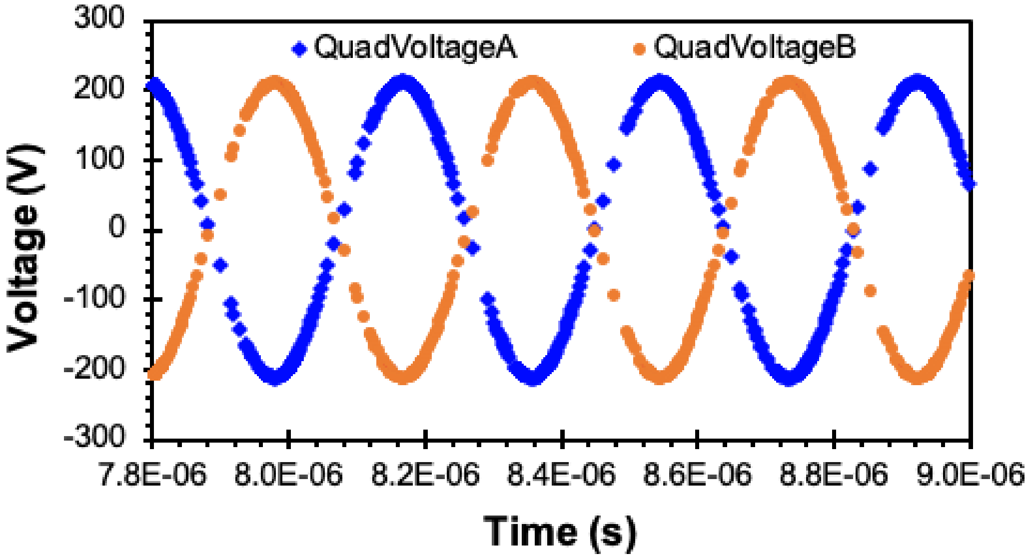

Figure 5-2: Simulation results of the 2.65 MHz RF voltage produced by the electronics shown in Fig. 5-1.

Fig. 5-1 shows the LTspice circuitry schematic in the full-bridge configuration and Fig. 5-2 shows the generated sinusoidal waves. From the simulations it was clear that in theory the circuitry would work. We also ran a Fourier analysis on the generated sinusoids to ensure that sine waves had little to no higher harmonics or distortion.

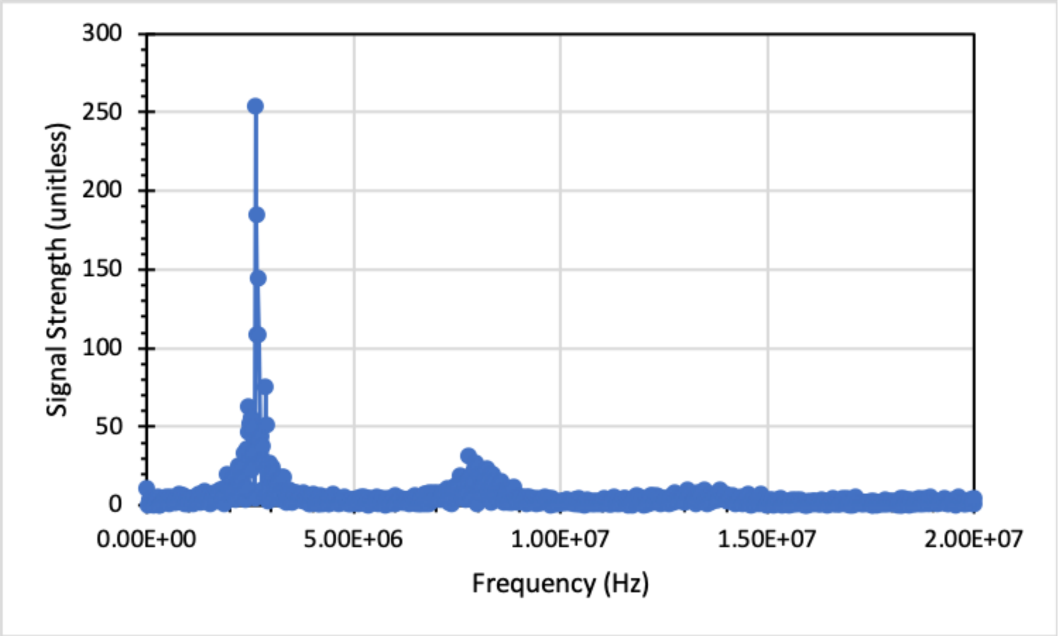

Figure 5-3: Fourier Transform of the simulation sinusoidal waves in Figure 5-2. A clear peak at 2.65 MHz. There are higher harmonics, but they are at least an order of magnitude lower in signal strength and decreasing in magnitude as frequency increases.

The Fourier analysis data in Fig. 5-3 was generated using a short, custom matlab script that first made the output data from LTSpice uniform and then computed the FFT (the code is included in the Appendix). This is necessary because LTSpice outputs data with non-uniform time steps in order to speed up computation and overall simulation speeds, which makes it difficult to compute the FFT directly.

Once the LTSpice was made linear we were able to compute the FFT shown above. We see a clear peak at 2.65 MHz, which is the frequency we specified. This peak is more than an order of magnitude above the next harmonic which is around 8 MHz and after this point there are not any visible harmonics. These results warranted continuing to the prototype stage of the electronics.

5.1.2 Initial Driving Electronics Circuitry

The general design flow of this circuit is described below in Figure 5-4.

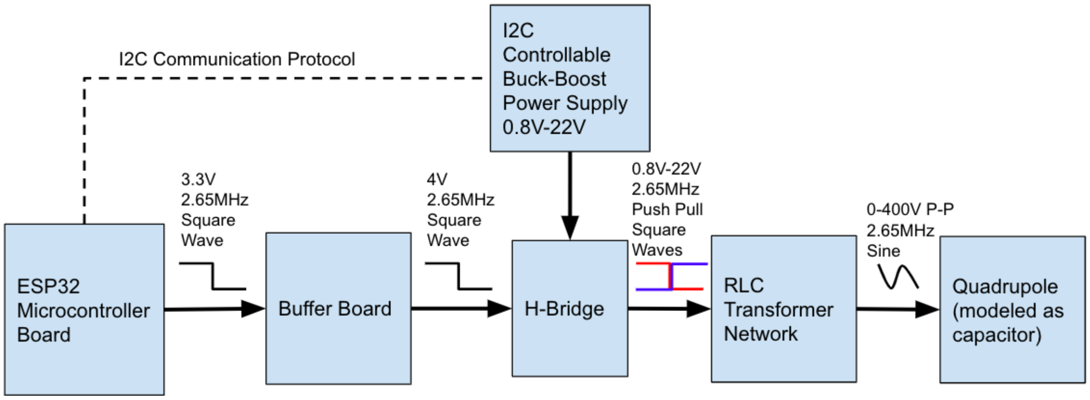

Figure 5-4: Basic circuit flow diagram.

Initial circuitry consisted of five separate circuits for more rapid implementation and iteration using a lab bench variable power supply instead of a small buck-boost converter (later we fix this issue and use a much smaller, controllable power supply). The boards that were designed and used are shown below.

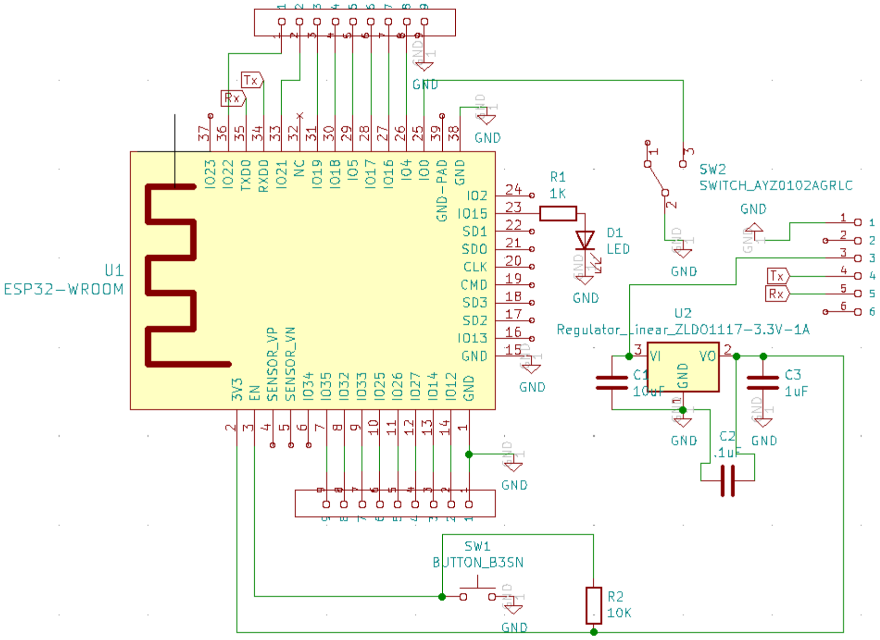

Figure 5-5: Main ESP32 Microcontroller Board w/ TTL interface for programming via a computer with a TTL to USB adapter.

The ESP32 is programmed using C++. For this project I take advantage of the digital output pins, PWM pins, and I2C communication ability of the microcontroller. The ESP32 also has Wi-Fi communication capability.

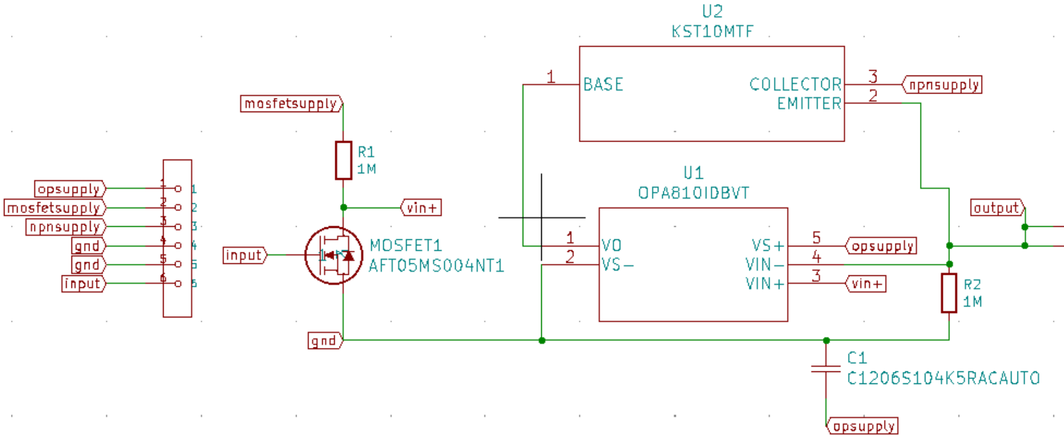

Figure 5-6: Buffer Board that takes the generated square wave from the ESP32 Microcontroller and then feeds it into the LTC7060 board in Fig. 5-7.

Fig. 5-7 and 5-8 are the LTC7060 and MOSFETs broken into two boards. Figure 5-9 combines both into one board and I compare the differences in performance of both approaches in 5.2.1 Sine Wave Generation Initial Tests.

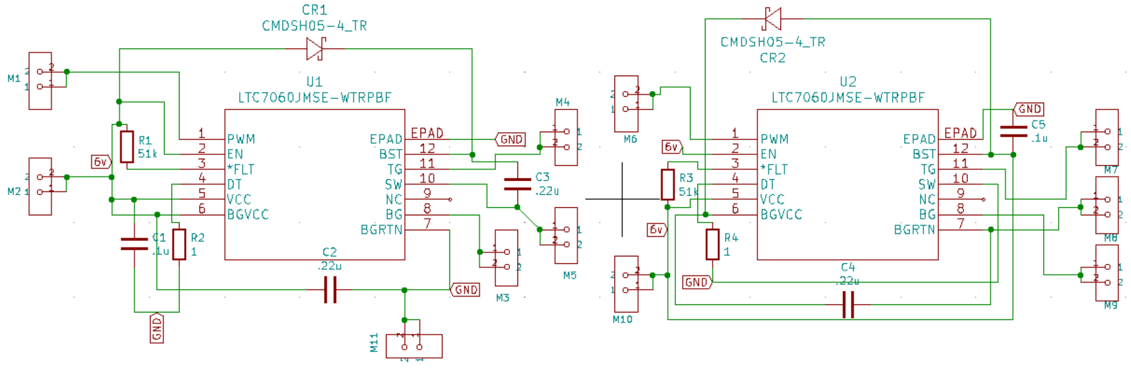

Figure 5-7: LTC7060 breakout board that then interfaces with the MOSFET driving board to drive all 4 MOSFETs.

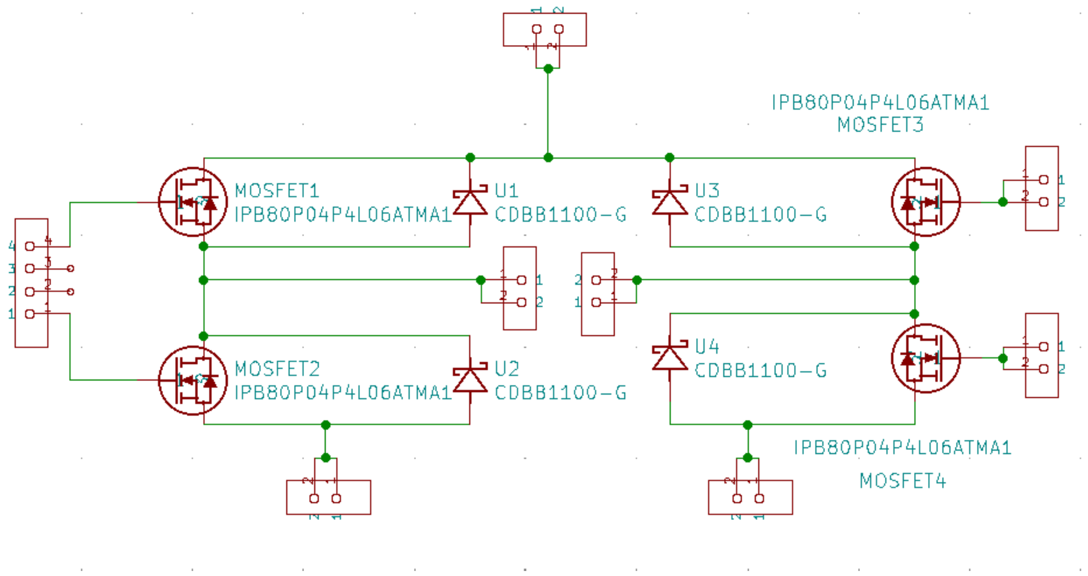

Figure 5-8: MOSFET Board that then drives the dual transformers and RLC circuits

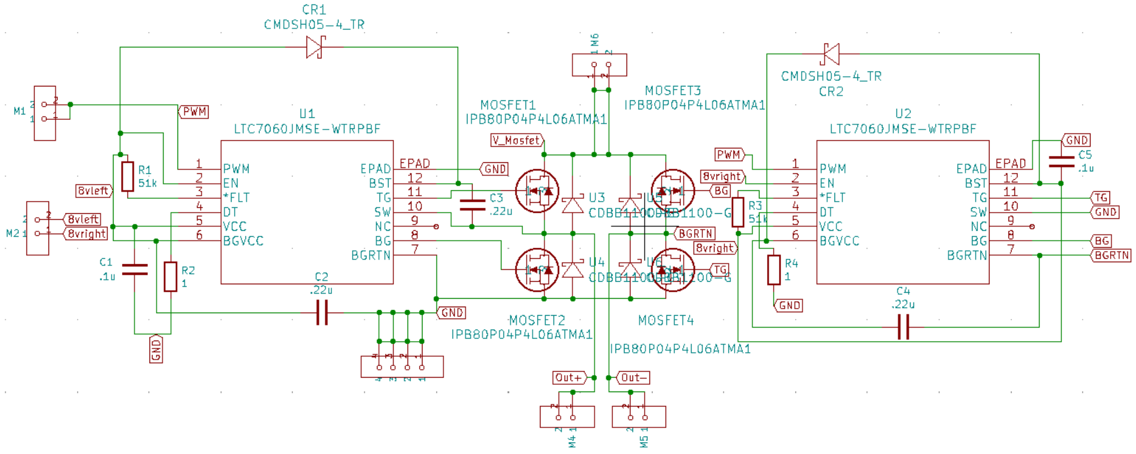

Figure 5-9: Combined PCB of the LTC7060 chips and the MOSFETs. This circuit is connected directly to the load circuit.

Fig. 5-9 is the combined PCB that interfaces the LTC7060 Board with the MOSFETs on one PCB. This decreases potential outside distortion of the signals. Furthermore, this board includes two ground planes that the initial two PCB boards do not have. These additional grounded planes greatly reduce the distortion of the generated square waves, which in turn removes distortion from the generated sine waves. Cleaner, less distorted sine waves, produce higher resolution mass spectra. The final part of the circuitry is the parallel transformer, series, RLC network that powers the quadrupole.

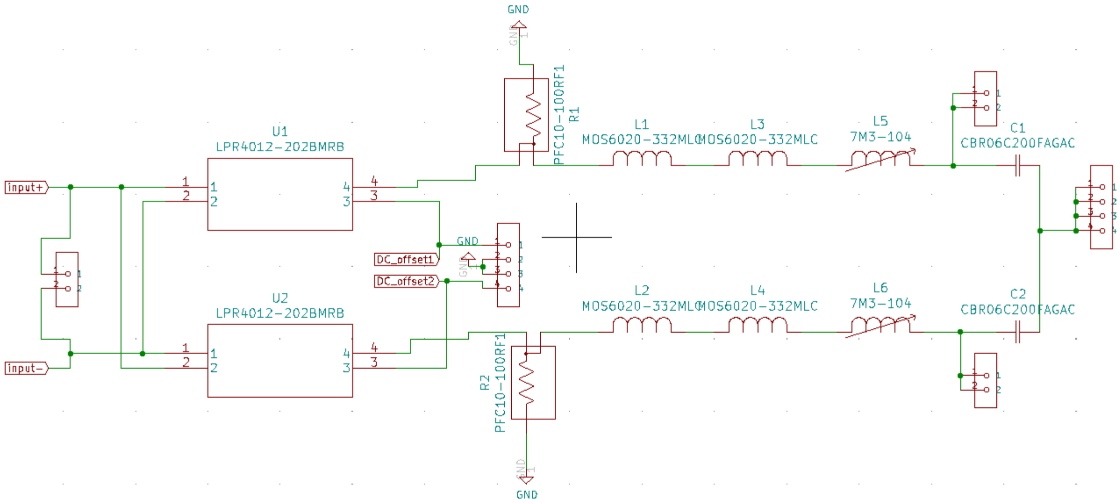

Figure 5-10: Parallel transformers to RLC network and load capacitors (which simulate the capacitive quadrupole load).

With the initial circuitry defined we go on to the testing and evaluation of the circuitry. The next section will show the difference in output power efficiency and output distortion of the MOSFET network between the two separated boards (Fig. 5-7 and 5-8) and the combined board with a grounded copper plane (Fig. 5-9).

5.2 Driving Electronics Testing and Evaluation

5.2.1 Sine Wave Generation Initial Tests

The two separated boards and the combined board are both tested to compare the power consumption at different frequencies, as well as the relative quality of the square waves that were generated by the full-bridges.

Frequency	Buffer (V)	Buffer (A)	Buffer (W)	7060 (V)	7060 (A)	7060 (W)
10KHz	6	.02	.117	8	.002	.018
100KHz	6	.02	.120	8	.009	.069
1MHz	6	.027	.160	8	.076	.609
2MHz	6	.034	.206	8	.150	1.199

Table 5.1: The current and wattage of the Buffer Board and two **separate** circuits (LTC7060+MOSFETs) with respect to increasing frequency. Negligible voltage/current applied to load.

Frequency	Buffer (V)	Buffer (A)	Buffer (W)	7060 (V)	7060 (A)	7060 (W)
10KHz	6	.02	.117	8	.002	.018
100KHz	6	.02	.121	8	.009	.069
1MHz	6	.027	.161	8	.071	.570
2MHz	7	.034	.252	8	.136	1.09

Table 5.2: The current and wattage of the Buffer Board and **combined** circuits (LTC7060+MOSFETs) with respect to increasing frequency. Negligible voltage/current applied to load.

From a power consumption perspective it is not exactly clear that the combined board performed better and there are only differences apparent near the 2 MHz range where the power consumption of the combined board is slightly lower than the non-combined board.

However, when we visually inspect the sinusoidal waves from the oscilloscope screenshots for these tests, it becomes clear that the combined board with the ground planes is performing significantly better. The generated square waves and sinusoidal waves are much cleaner and contain less ringing and harmonics. The oscilloscope graphs for all 8 tests are shown below side by side for each frequency.

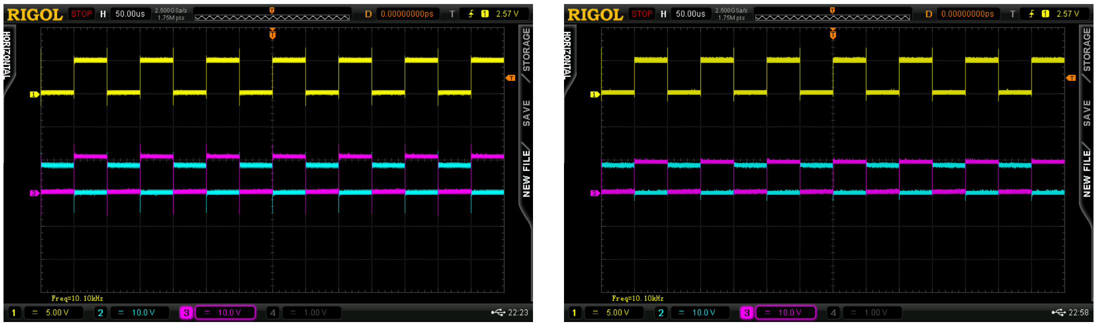

(a) 10KHz Separate Boards

(b) 10KHz Combined Board w/ GND Plane

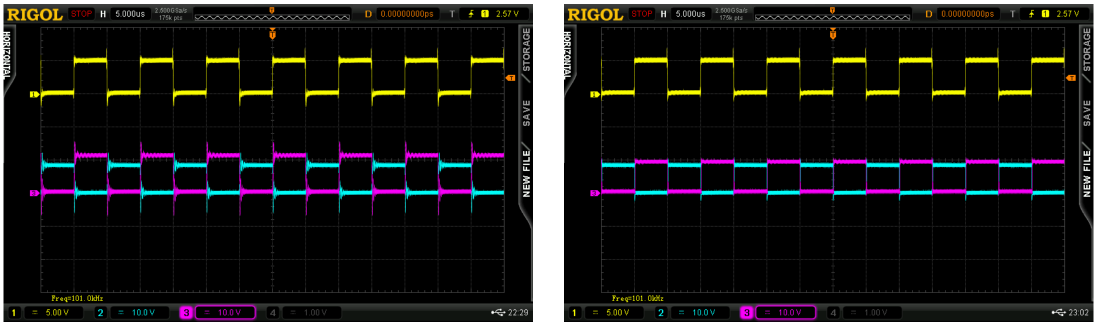

(c) 100KHz Separate Boards

(d) 100KHz Combined Board w/ GND Plane

(e) 1MHz Separate Boards

(f) 1MHz Combined Board w/ GND Plane

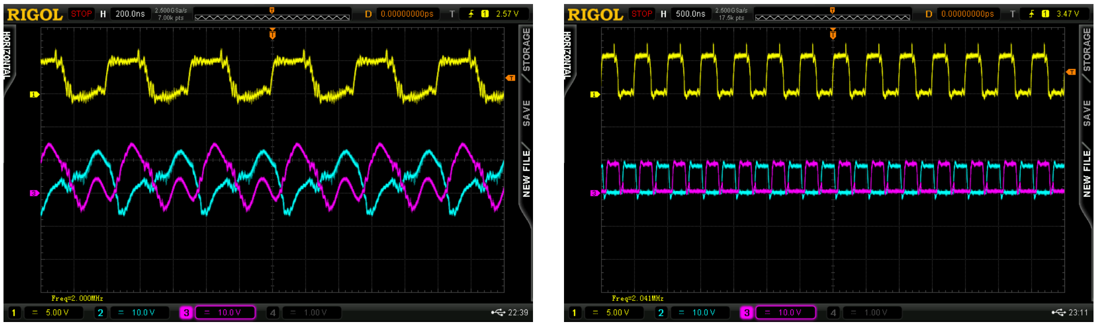

(g) 2MHz Separate Boards

(h) 2MHz Combined Board w/ GND Plane

Figure 5-11: Yellow is the driving frequency from the ESP32. Blue and magenta are the output of the full-bridge circuit w/out the quadrupole capacitive load.

The next step was feeding the square waves to the load circuit. Now that the square waves retain their form even at the higher frequencies, we fed them to a transformer w/ 1:4 voltage step-up and 12 MHz SRF (332G-NA5880-AE Coupled Inductor), which breaks up the signal into two RLC series networks with these components: 10 ohm resistor, 7M3-333 variable inductor (33 uH nominal 25-41 uH), MOS6020-473ML (47 uH), MOS6020-154ML (150 uH), a 10 ohm resistor and two 12 pF capacitors in series (because of the shape of the pcb board the capacitance measured across these two capacitors with an LCR meter at 1 MHz and 1 V amplitude was 19 pF).

The following graphs in Fig. 5-12 show the sinusoidal amplitude across the capacitors. Each graph displays the amplitude as a function of the MOSFET driving voltage from 0 to 4.5 V which shows the ability of the circuit to perform in the 0-400 V_{pp} amplitude range even despite some shortcomings in measurement that I discuss afterwards.

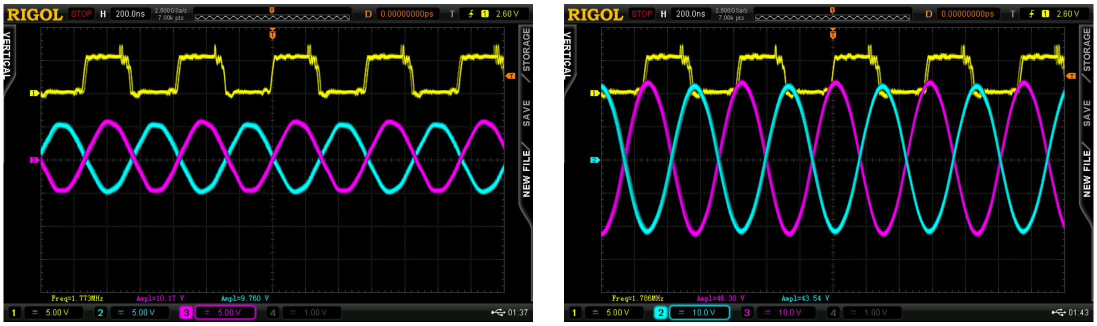

(a) 10V RF P-P
(b) 44V RF P-P

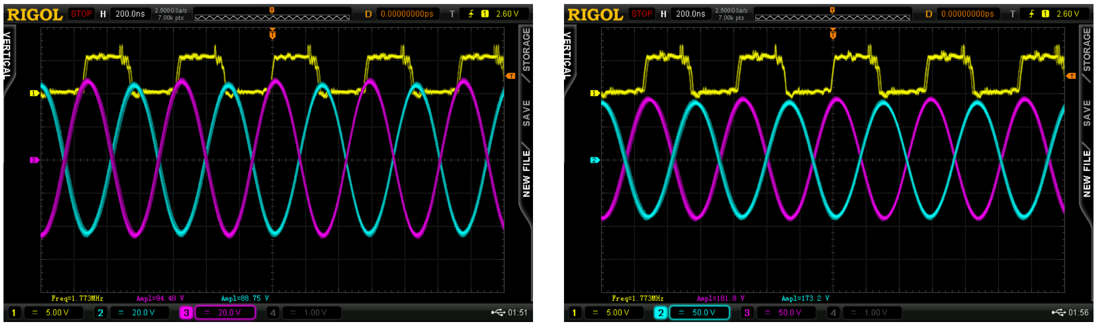

(c) 90V RF P-P
(d) 175V RF P-P

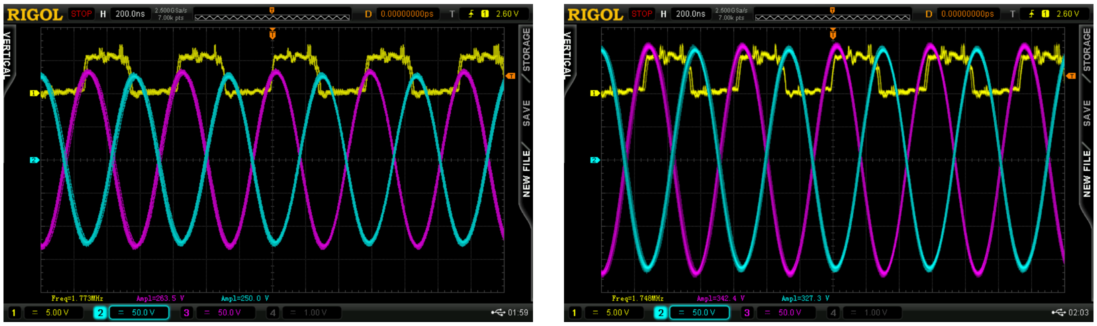

(e) 255V RF P-P
(f) 335V RF P-P

(g) 380V RF P-P

Figure 5-12: Yellow is the driving frequency from the ESP32 (1.77 MHz). Blue & magenta are the sinusoidal output across the load capacitance. For all of these graphs: Buffer board was driven at 6.4 V consuming .33 A & .24 W; 7060 Board was driven at 7 V consuming .109 A & .762 W.

*F*ig.	MOSFET(V)	MOSFET(A)	MOSFET(W)	Sine1 P-P (V)	Sine2 P-P (V)	Total Watts (W)
a	.0	.000	.000	10.17	9.76	.972
b	.5	.024	.012	46.30	43.54	.984
c	1	.060	.060	94.48	88.75	1.032
d	2	.125	.251	181.80	173.20	1.223
e	3	.187	.563	263.50	250.00	1.535
f	4	.252	.999	342.40	327.30	1.971
g	4.5	.286	1.286	384.10	371.60	2.258

Table 5.3: This table shows all the additional information regarding power, applied voltages, etc. to achieve Fig. 5-12 a-g

These tests demonstrate the ballpark figures of 0-400 V_{pp} w/ relatively low wattage (max of 2-3 W). These measurements are satisfactory as estimates, however, the probes that are in use have a capacitance of ∼12 pF which makes these measurements skewed (actual measurement of the voltage across the capacitors is likely higher). Therefore, later in the chapter I discuss how I measured the actual voltages across the capacitive loads and also how this increased the voltage amplitudes and led to decreased power consumption.

The following picture shows the testing setup that we used for the previous tests. There are 2 exceptions: in previous tests the quadrupole was not attached and the oscilloscope probes were hooked directly across the capacitive load—which gave us the high power consumption we noticed in the above tables (in previous tests the quadrupole was approximated with capacitors; In future tests we run across the quadrupole itself).

5.2.2 Sine Wave Generation Across Quadrupole

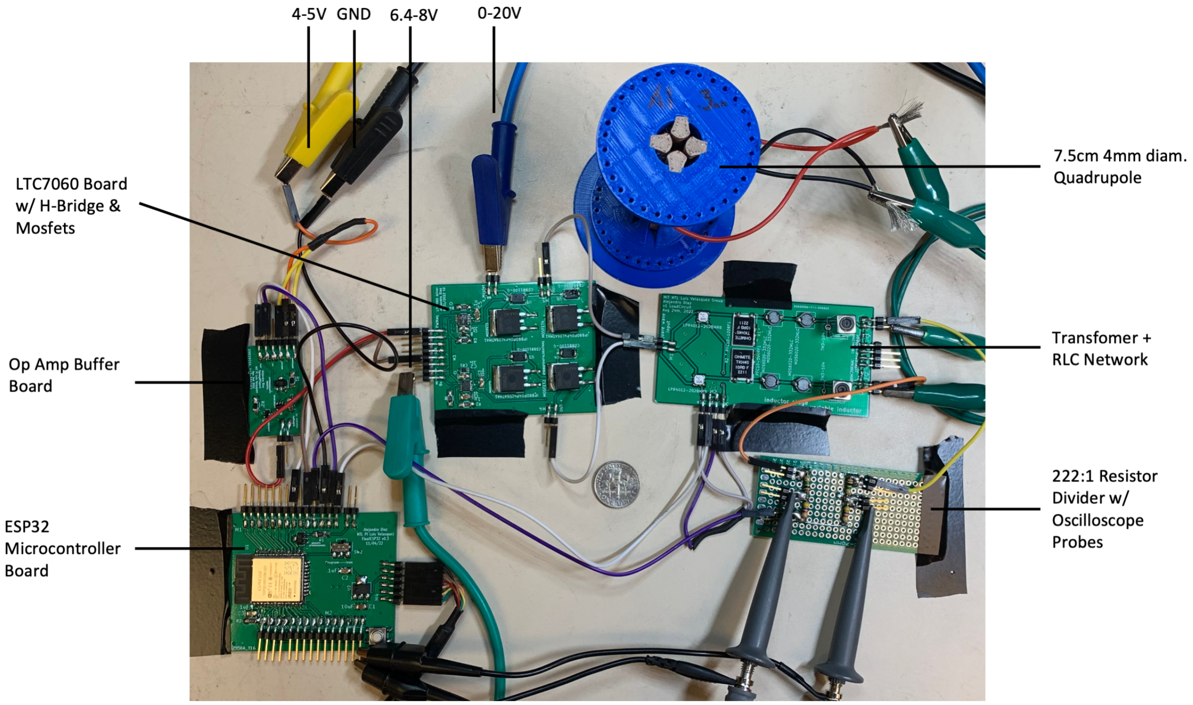

Figure 5-13: Circuitry Setup with all of the boards using power supply connections to vary the amplitudes of the sinusoidal waves.

With the exact setup above we took some preliminary data. The differences from the previous tests are that the quadrupole is actually included in the test (the quadrupole is in parallel with 12 pF capacitance—measured with an LCR meter at 1 MHz, 1 V amplitude, the total capacitance is 35 pF). Also we measure amplitude across a resistor network consisting of 1.04M ohms to 4.7K ohm resistor dividers (we multiply what's on the oscilloscope by 224).

MOSFET (V)	MOSFET (A)	MOSFET (W)	Osc. Vpp (V)	Sine Vpp (V)	Total Watts (W)
.3	.000	.000	.24	53.76	.500
.5	.005	.002	.35	78.40	.502
1.0	.024	.024	1.00	224.00	.524
1.5	.042	.064	1.65	369.60	.542
2.1	.060	.127	2.00	448	.560

Table 5.4: LTC7060 board at 6.6 V (runs at .061 A and .4 W). Buffer board at 4 V (.025 A .1 W). Total Watts above is .4 W + .1 W + MOSFET (W).

As you can see above, the power requirements to achieve the same sinusoidal amplitude are now much lower (given the oscilloscopes probes are no longer affecting the capacitance of the RLC network). For the amplitude of $\sim V_{pp}$ previously >2.26 W was required vs. .56 W.

For the final tests, in order to control the amplitude of the sinusoidal waves, the TPS55289 Buck-Boost Converter Evaluation Board (Fig. 5-14) from Texas Instruments is interfaced with the ESP32 using the I2C protocol to have two controllable voltage supplies ranging from .8-22 V. One supply is for the DC offsets so that the quadrupole resolves. The 2nd buck-boost converter supplies the MOSFET network and controls the amplitude of the sinusoidal RF waves.

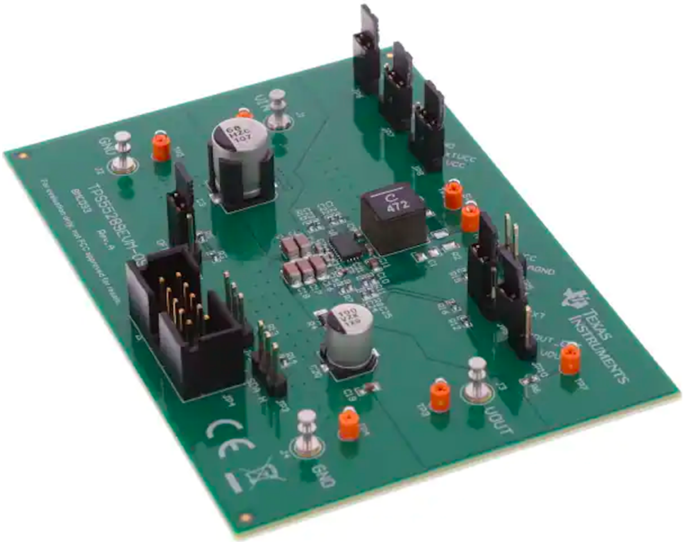

Figure 5-14: TPS55289 Buck-Boost Converter Evaluation Board to produce voltages from .8 V to 22 V [5.3]

Below is the combined circuitry for the ESP32, Buffer Board and MOSFET Full Bridge.

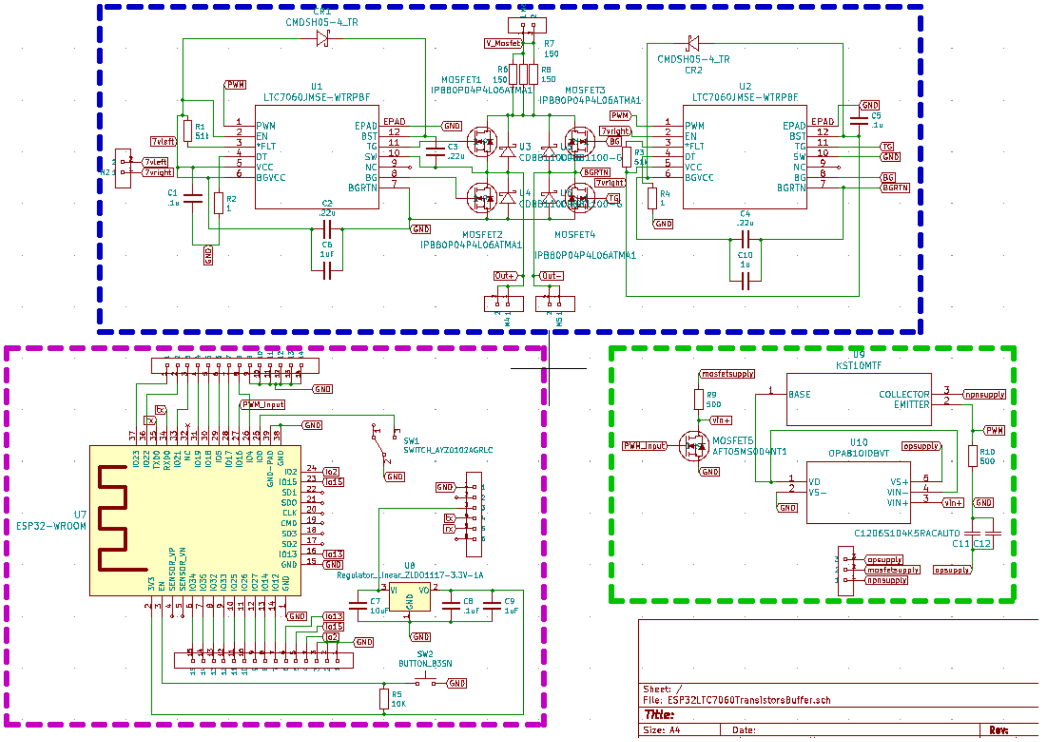

Figure 5-15: Overall Circuitry: Combined ESP32, Buffer Circuitry, and MOSFET full-bridge.

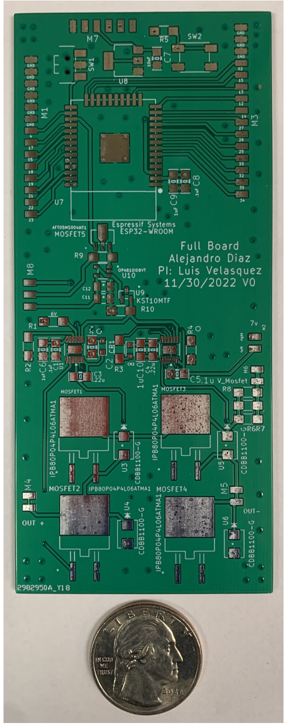

Figure 5-16: Overall Circuitry: Combined ESP32, Buffer Circuitry, and MOSFET full-bridge PCB. US Quarter for reference.

Next we run the combined circuitry shown above with the setup in Fig. 5-13. We switch out the left hand side of the setup in Fig. 5-13 for this single combined board. For this final test we also use the TPS55289 to provide DC offsets and vary the sinusoidal RF amplitude.

The code we use for this final run is included in the linked git repository in the appendix (variations of this code were used for previous electronics tests). In essence the code commands the ESP32 to generate a 1.35 MHz signal that is fed to the buffer circuit and then the ESP32 is told to communicate via I2C with the two TPS55289 boards to increase the RF and DC amplitudes over time (the TPS55289boards have 2048 steps within their voltage range making the output resolution adequate as explained at the start of this chapter). More info is in the commented code in the Appendix.

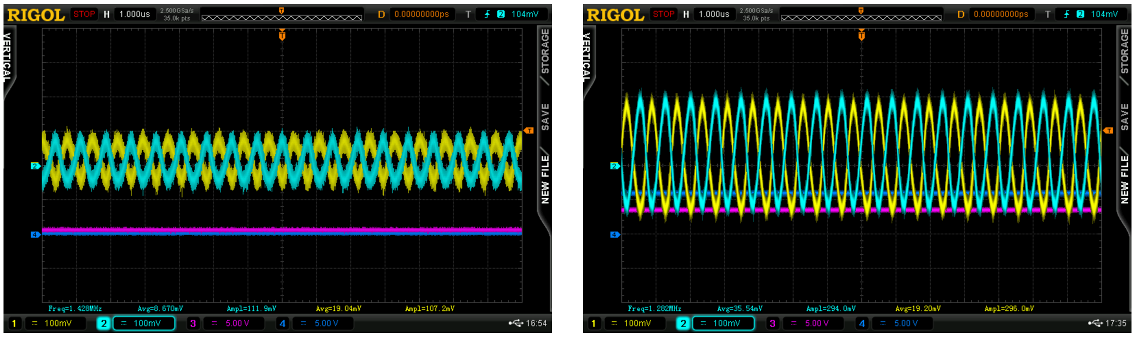

(a) 0V applied .004A .023W **22V RF P-P** (b) 3.5V applied .015A .073W **66V RF P-P**

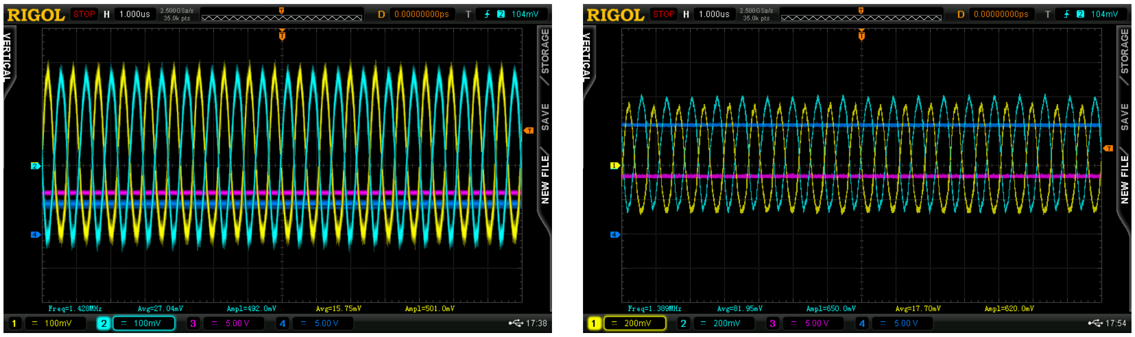

(c) 6V applied .047A .235W **110V RF P-P** (d) 8.5V applied .105A .526W **143V RF P-P**

(e) 9.5V applied .136A .683W **164V RF P-P**

Figure 5-17: For all of these graphs: Buffer circuitry was driven at 3.8 V and consumed .022 A and .084 W; LTC7060 circuitry was driven at 7 V and consumed .04 A and .277 W. Each graph is captioned with the TPS55289 output voltage (wattage and amperage used for both TPS55289 is also shown—both supplies powered by 5 V via in-house power supply) and resulting RF P-P voltage. Sinusoidal waves are measured across quadrupole with 224:1 resistor network. Blue line is DC offset. Purple line is DC sinusoidal amplitude voltage supply.

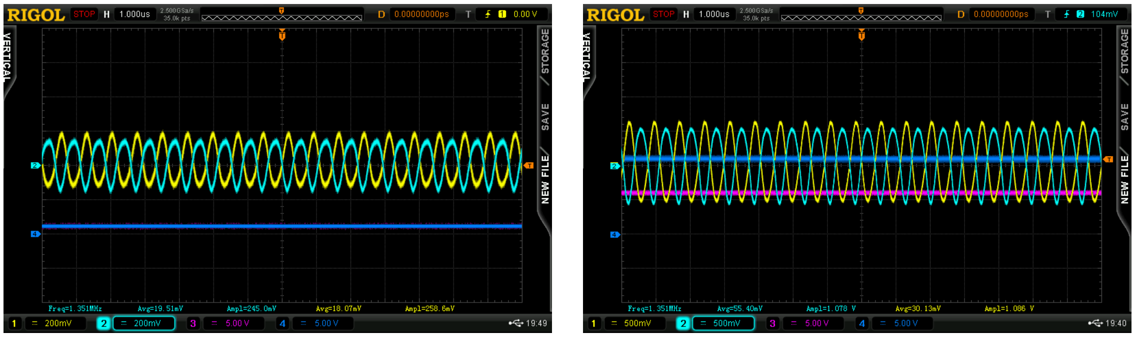

(a) 0V applied .002A .010W **56V RF P-P** (b) 6V applied .041A .204W **241V RF P-P**

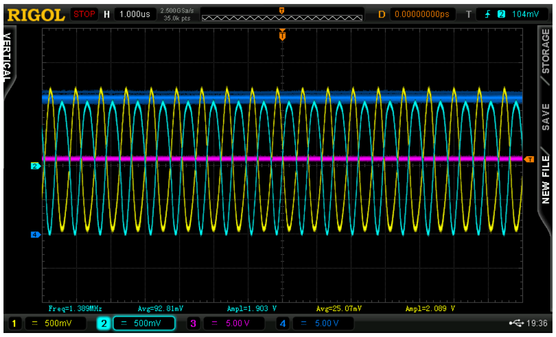

(c) 11V applied .157A .786W **448V RF P-P**

Figure 5-18: For all of these graphs: Buffer circuitry was driven at 3.8 V and consumed .022 A and .084 W; 7060 circuitry was driven at 7 v and consumed .04 A and .277 W. Each graph is captioned with the TPS55289 output voltage (wattage and amperage used for both TPS55289 is also shown—both supplies powered by 5 V via in-house power supply) and resulting RF P-P voltage. Sinusoidal waves are measured across quadrupole with 224:1 resistor network. Blue line is DC offset. Purple line is DC sinusoidal amplitude voltage supply.

Between Fig. 5-17 and Fig. 5-18 we achieved between 22-448 V P-P. The difference between the figures being that Fig. 5-17 has reduced EMI by twisting the measurement wires together and Fig. 5-18 does not. Due to issues with the buck-boost converters (TPS55289EVM-093) and what was likely some load issue the voltages maxed out at 164 V_{pp} and 448 V_{pp} respectively. This was also with a 100 ohm resistor in series with the output of the buck-boost converter that fed the full-bridge (this meant significant power loss, but the converters would not operate otherwise—unclear why this was the case).

Earlier in Table 5.4 we showed that with the in-house power supply we were able to achieve up to 448 V with only .127 W, but with the TPS55289EVM-093 we used .786 W (nearly a tenfold increase). It is clear there is an issue with our variable DC power supply (TPS55289EVM-093). However, this was not the main focus of the electronics as variable DC power supplies are much more studied and not as difficult or novel to implement and we showed the electronics work at low wattage and current draw with our in-house power supply.

For these electronics to work well within an integrated system there are future steps that should be taken. Obviously the variable buck-boost converter we used was faulty (unclear whether user error or limitations of the device). The current DC bias has a range of .5-22 V. The DC bias should be from -34 to +34 V to have the correct ratio RF/DC (∼12) to support RF voltages up to the 400 V we specified earlier (this could be two simple boost converters with variable resistors to output different voltages—Zoey Bigelow in our lab constructed such a circuit to provide -50 V and +50 V rails and this is included in the Appendix). Feedback for the DC and RF amplitudes would make the system more precise. Finally, control of the ionizer, ion optics and a current measurement device would be necessary. A colleague (Javier Izquierdo Reyes) has used the ADL5303 [5.4] as a current measuring device, which is capable of measuring as low as 100 pA (which can possibly interface with our quadrupole setup given we attained peaks of 250 pA; however, we would desire better ion optics tuning/setup or other transmission heightening techniques). Otherwise, more sophisticated current amplifying/measuring devices could be implemented and interfaced.

5.3 References

[5.1] Cheung, K. "Chip-Scale Quadrupole Mass Filters for a Micro-Gas Analyzer", 2009.

[5.2] E. G. Kilinc, K. Ture, F. Maloberti and C. Dehollain, "Design and comparison of class-C and class-D power amplifiers for remotely powered systems," 2013 IEEE 20th International Conference on Electronics, Circuits, and Systems (ICECS), Abu Dhabi, United Arab Emirates, 2013, pp. 461-464, DOI: 10.1109/ICECS.2013.6815454

[5.3] Digikey, *TPS55289EVM-093*, accessed January 2023, `https://www.digikey.com/en/products/detail/texas-instruments/TPS55289EVM-093/16516664`

[5.4] Analog Devices, *ADL5303*, accessed January 2023, `https://www.analog.com/en/products/adl5303.html#product-overview`

Chapter 6 Conclusion and Future Work

6.1 Discussion

We developed the first compact, monolithically 3D-printed, RF quadrupole mass filters via extrusion using PLA (dielectric parts) and PLA doped with copper nanoparticles (conductive parts). The quadrupoles were functional and we detected argon at mass 40 with a resolution of 5 and mass range of 1-250 amu. There were also promising results for the detection of FC-43 (Ch. 4).

The low-power driving electronics for the quadrupole mass filter achieved the important characteristics we defined at the beginning of this thesis: operation under 3 watts and two 180 degree out-of-phase sinusoids that can be varied and increased up to 400 V_{pp}.

We have shown that quadrupoles can be monolithically 3D-printed using relatively inexpensive materials all while consuming relatively little power, (<3 W) which is advantageous for space and deployability into in-situ, portable, and hand-held scenarios, e.g., drones, CubeSats. The lowered cost of manufacture may allow for greater proliferation of mass spectrometers, instruments that are normally confined to well-funded chemical laboratories. This work provides an opportunity for more precise, low-power, deployable, and compact mass spectrometry systems.

6.2 Future Work

With regards to the **manufacturing process**, extrusion printing shows promise, but has accuracy limitations and is limited by extrusion temps and overhanging structures among other things. We did not exhaust the parameter space for extrusion with multiple materials—the first parameters to optimize might be extrusion temps, printing chamber humidity/temperature, retraction distances and printing speeds. Furthermore, we experimented with nickel and copper plating in Ch. 3 with promising results. Future work could explore copper plating to enhance the characteristics of the Electrifi filament. Nickel plating could be used to plate PLA or possibly other materials such as PEEK without the need for conductive filament—in this case other printing methods could be used such as DLP etc.

We can also improve the **quadrupole configuration/setup**. One idea would be to instead create a triple quad mass spectrometer with two quadrupole mass filters and a collision cell [6.1]. Higher resolution is attained with a triple mass spec vs. our single quad setup and would require few additional connections (but increased power, volume, and mass requirements). Another solution is improving the ion optics to better focus the ions into the quadrupole and out into our current measuring devices. More compact Einzel lenses can be used at either end of the quadrupole and voltages for all the stages can be fine tuned. Additionally these ion optics stages/Einzel lenses could also be monolithically 3D printed (making the manufacturing/assembly stages faster, more cost-efficient, and more compatible with in-space manufacturing)

There are also **alternate methods of driving the quadrupole mass filter**. Instead of varying the RF amplitudes, the frequency can be varied to achieve the same mass spectrum scanning [6.2], which would heavily reduce the RF amplitude requirement and could work readily with our system given the electronics can control the driving frequency via code. There are also alternate stability regions to operate within that should achieve higher resolutions at the expense of more power [6.3].

In order to improve our **quadrupole driving electronics** there are several avenues: adding feedback for the voltage amplitudes to more accurately control the voltages, adding more filtering/shielding to produce sine waves with less harmonics, and adding in more battery saving techniques, both in code and in the physical PCB. More suggestions are at the end of Ch. 5. If these electronics are sent to space, future work will have to interface the micro-controller with other electronics/power supplies onboard the satellite. Furthermore, all of the electronics can be made more compact (important for space considerations). The buck boost power supplies have many test points and prototyping features, and thus the footprint and weight can be greatly reduced. The additional electronics are not optimally compact on the PCB and have many additional test points/connections that can be removed as well.

6.3 References

[6.1] Yost R. A. (2022). The triple quadrupole: Innovation, serendipity and persistence. Journal of mass spectrometry and advances in the clinical lab, 24, 90–99. DOI: 10.1016/j.jmsacl.2022.05.001

[6.2] Wilamowski, B., et al., IECON'01. 27th Annual Conference of the IEEE Industrial Electronics Society (Cat. No.37243), "Enhancing The Sensitivity of Miniaturized Quadrupole Mass Spectrometers", DOI: 10.1109/iecon.2001.976470

[6.3] D. J. Gershman, B. P. Block, M. Rubin, M. Benna, P. R. Mahaffy, and T. H. Zurbuchen. Higher order parametric excitation modes for spaceborne quadrupole mass spectrometers. Rev. Sci. Instrum. 82, 125109 (2011). DOI: 10.1063/1.3669781

Appendix A Appendix

A.1 Git Repository for Longer Code etc.

`https://github.com/alejandrodiazz/MIT_Thesis_Appendix`

A.2 Additional Circuitry Approach

Initially we had difficulty implementing the Full H-Bridge design described in Ch. 5 so we looked into other options to generate the sinusoidal waves without an h bridge (and therefore, unfortunately also using more power). This approach is conceptually more simple and is outlined in this section.

We used the Buffer Board from Figure 5-6 to directly drive the transformer network with a variable resistor in series in order to control the current driven across the transformer and thus control the amplitude of the sinusoidal wave. The circuit was quickly modeled in Falstad as shown below in Figure A-1.

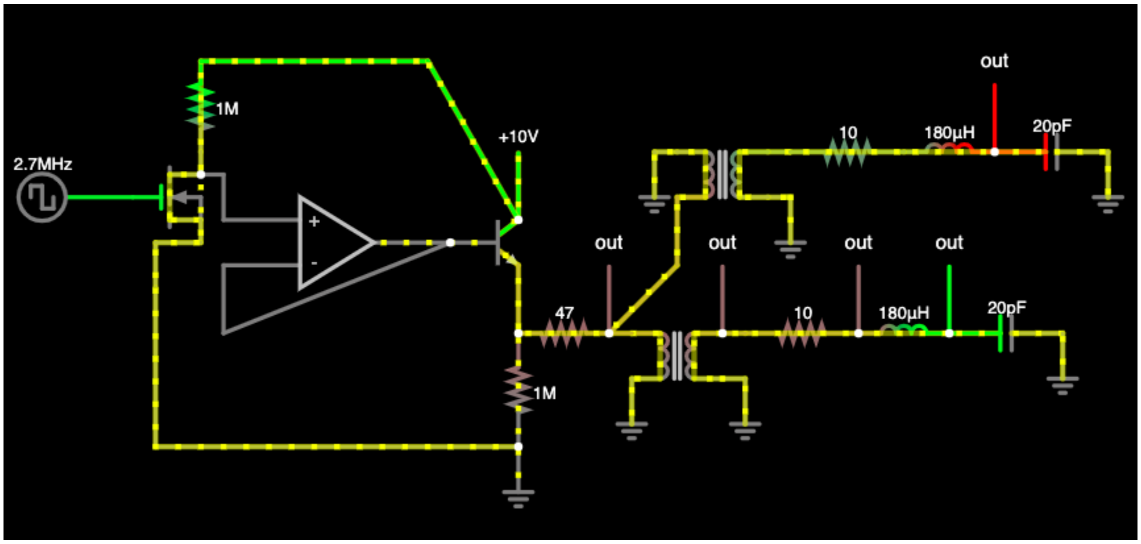

Figure A-1: Falstad simulation of circuit with variable resistor. The 47 ohm resistor in this simulation will be varied in practice to achieve varying sine amplitude across the quadrupole. Simulation file text is in the code appendix.

The difficulty in this solution is the variable resistor. Three options were considered.

1. IC variable resistor chips
2. Motor/servo controlled potentiometer
3. Resistor array indexed through de-multiplexers and n-mosfets

For option 1 the deciding factors were: the Falstad simulation shows that up to 200 mA runs through the variable resistor at max sinusoidal amplitude and that the resistance should go up to at least 1k ohms to achieve low enough sinusoidal amplitudes. This meant that given IC variable resistor chips have relatively low current ratings (∼25 mA), a repetitive parallel and series network of many variable resistor chips along with their communication lines would have to be designed. This caused us to discount option 1.

Option 2 we discounted on the basis of power consumption and the added complexity of additional motor control circuitry (however in retrospect it could be revisited).

Thus we settled on option 3. Even though it is redundant and repetitive it seemed the easiest from a design perspective. The circuitry is shown below in Figure A-2.

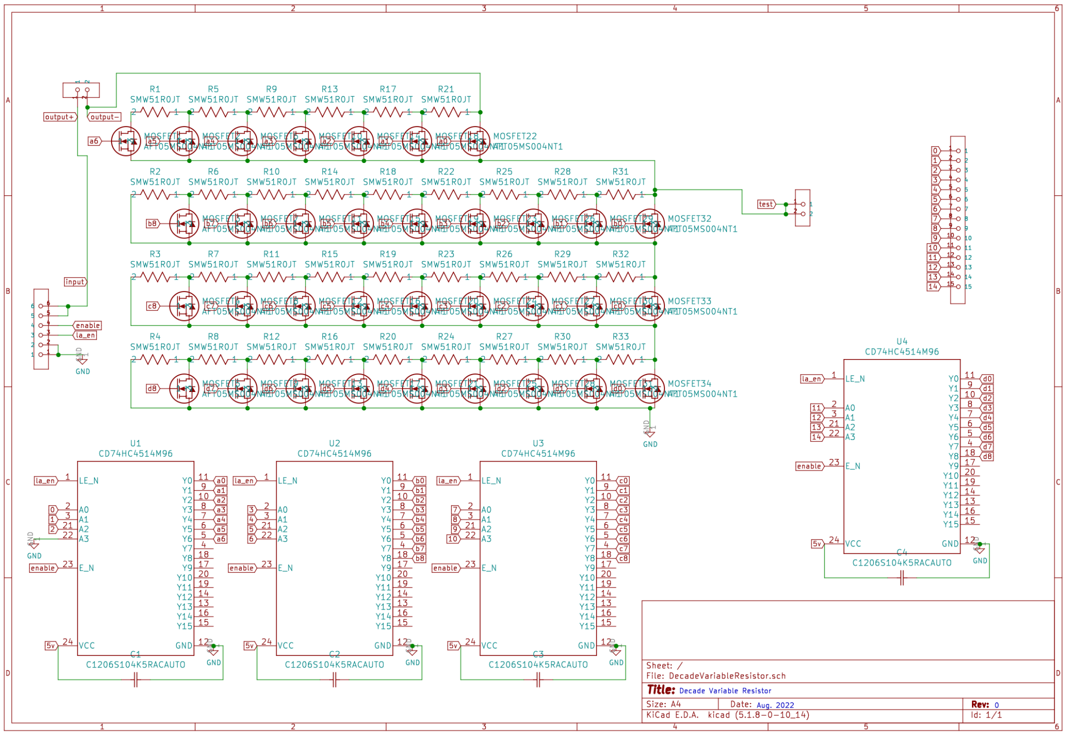

Figure A-2: Kicad schematic of a Decade Variable Resistor

While this design worked and generated variable sinusoidal amplitudes in tandem with the other circuitry—there were issues at low resistances with the traces contributing significant relative resistance that made it difficult to control fine tune adjustments to the sinusoidal amplitude. For this reason, as well as the larger volume of this circuit (10x more volume than the Full-Bridge) and higher power consumption, this design was forgone in lieu of the previously discussed Full-Bridge Design.

A.3 +- 50V Rail via Boost Converters

This circuit was created by a colleague (Zoey Bigelow). The original eagle file is included in the git repository linked above. GND2 is the +25V output and is used to reference the upper left circuit (which creates another +25V) and brings the final output up to +50V.

Same exact thing goes for GND3—except that it outputs the -25 V that is used to reference the upper right circuit (which drops the total to -25 V) and creates that final output of -50 V. The chip used is the MAX629.

To use this circuit as the variable DC supply for this project, two variable resistors would be attached to the outputs of the +-50 V outputs and the taps would be the output of either 0 to -50 V or 0 to +50 V. The variable resistors would be controllable via the ESP32.

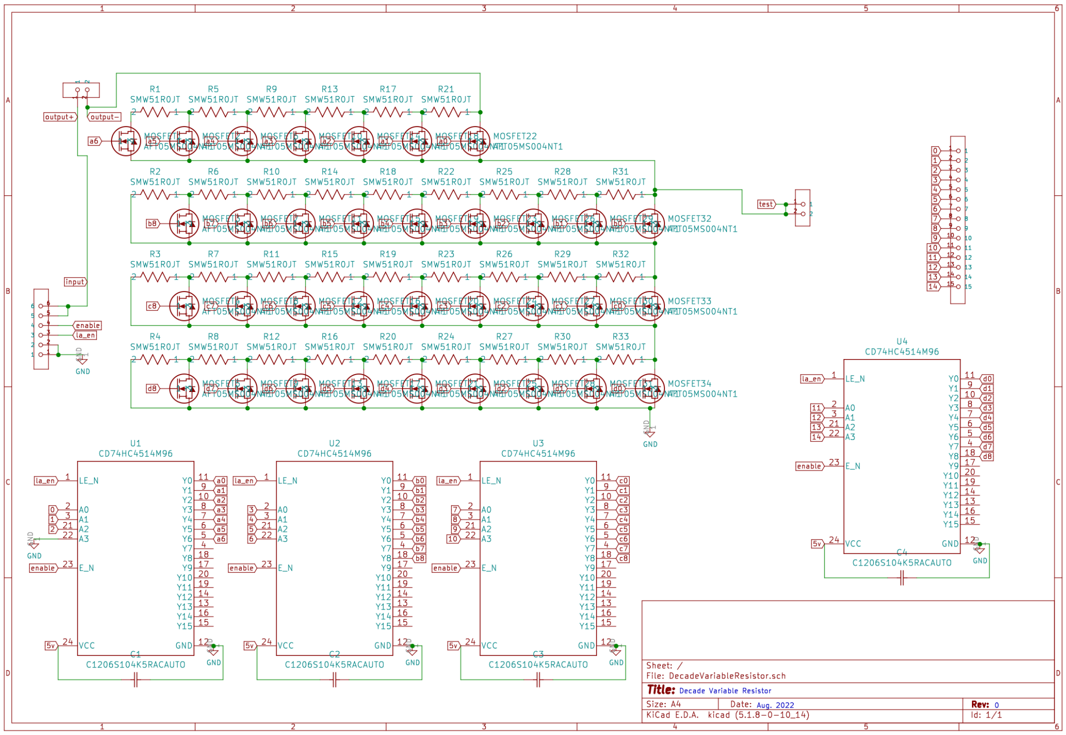

Figure A-3: +- 50V Rail via Boost Converters.

A.4 Matlab Normalization and FFT code

```
% the .txt file in this example had no column names
% and three fields, the first was the time in scounds
% and the following two were the voltage amplitude of
% two out of phase sinusoids (only the second column
% is analyzed)
fidi = fopen('sines1.txt', 'rt');
```

```
T_EMG = textscan(fidi, '%f%f%f', 'Delimiter','');
t = T_EMG{1};
EMG = T_EMG{2};
extra = T_EMG{3};
L = length(t);
Ts = mean(diff(t));                                 % Sampling Time
Fs = 1/Ts;                                          % Sampling Frequency
Fn = Fs/2;                                          % Nyquist Frequency
FEMG = fft(EMG)*2/L;                                % Fourier Transform (Normalised)
Fv = linspace(0, 1, fix(L/2)+1)*Fn;                 % Frequency Vector
Iv = 1:length(Fv);                                  % Index Vector
figure(2);
plot(Fv, abs(FEMG(Iv)));
grid;

endgame = [rot90(rot90(rot90(Fv))), abs(FEMG(Iv))];
writematrix(endgame,"simulationFourier2.csv");
```

A.5 Falstad Simulation Text for Variable Resistor Circuit

```
$ 1 1.5625000000000003e-8 0.37936678946831776 84 5 50 5e-11
t 272 96 320 96 0 1 -9.999800011230398 0.18485085132911108 1000 default
w 112 112 112 160 0
R 320 80 320 16 0 0 40 10 0 0 0.5
r 480 160 560 160 0 10
l 560 160 624 160 0 0.00017999999999999998 -0.02870667920692416 0
r 320 160 320 240 0 1000000
g 320 240 320 272 0 0
```

```
c 624 160 704 160 0 2e-11 -38.72201382908781 0.001

g 704 160 704 192 0 0

a 112 96 272 96 9 20 -20 1000000 0.00019998876960117514 0.00019999076948887116 100000

w 320 112 320 160 0

r 320 160 384 160 0 47

r 96 -32 96 32 0 1000000

w 64 128 64 96 0

f 48 64 96 64 32 1.5 0.02

w 96 80 96 96 0

w 96 96 64 96 0

R 48 64 -16 64 0 2 2650000 2 2 0 0.5

w 112 80 112 48 0

w 112 48 96 48 0

w 96 48 96 32 0

w 96 -32 256 -32 0

w 256 -32 320 80 0

w 64 128 64 240 0

w 64 240 320 240 0

T 400 160 464 160 0 0.000002 1 9.239253782877821e-8 0.028706679206924157 0.999

g 400 192 400 224 0 0

w 384 160 400 160 0

w 464 160 480 160 0

w 480 192 464 192 0

O 624 160 624 96 0 0

O 656 32 656 -32 0 0

w 512 64 496 64 0

w 496 32 512 32 0

w 416 32 432 32 0

g 416 32 416 64 0 0

T 432 32 496 32 0 0.000002 1 -9.239191109400302e-8 -0.028706679206924567 0.999
```

```
g 736 32 736 64 0 0

c 656 32 736 32 0 2e-11 38.722013829086826 0.001

l 592 32 656 32 0 0.00017999999999999998 0.028706679206924542 0

r 512 32 592 32 0 10

w 384 160 432 112 0

w 432 112 432 64 0

w 112 160 272 96 0

O 384 160 384 96 0 0

O 464 160 464 96 0 0

O 560 160 560 96 0 0

g 480 192 480 224 0 0

g 512 64 512 96 0 0

o 30 1 0 4098 160 0.1 0 1

o 31 1 0 4098 160 0.1 1 1

o 10 1 0 4099 10 0.4 2 2 10 3

o 44 1 0 4098 10 0.1 3 1

o 27 1 0 4099 10 0.2 4 2 27 3

o 46 1 0 4098 10 0.1 5 1

o 45 1 0 4098 10 0.1 6 1

38 4 F1 0 0.000312 0.00031299999999999996 -1 Inductance
```

A.6 Printing Parameters Appendix

*P*arameter	Conductive Filament	Non-Conductive Filament
Extruder		
Nozzle Diameter	.5 mm	.5 mm
Extrusion Multiplier	.95	.97
Extrusion Width	.40 mm	.40 mm
Retraction Distance	.00 mm	2.00 mm
Extra Restart Distance	.00 mm	-.03 mm
Retraction Vertical Lift	.50 mm	1.00 mm
Retraction Speed	800 mm/min	4000 mm/min
Coasting Distance	.00 mm	.03 mm
Wipe Nozzle	n/a	n/a
Layer		
Primary Extruder	left extruder (T0)	right extruder (T1)
Primary Layer height	1.0 mm	.3 mm
Top Solid Layers	8	6
Bottom Solid Layers	6	6
Outline Perimeter Shells	2	2
Outline Direction	inside-out	inside-out
Print Islands Sequentially...	no	no
Single Outline Corkscrew...	no	no
First Layer Height	100%	110%
First Layer Width	100%	110%
First Layer Speed	20%	10%

Table A.1: Printing parameters for conductive vs. non-conductive filament. Full profiles for conductive and non-conductive filament are in the 2nd appendix.

*P*arameter	Conductive Filament	Non-Conductive Filament
Additions		
Skirt Layers	2	3
Skirt Offset from Part	0 mm	0 mm
Skirt Outlines	4	15
Infill		
Infill Fill Pattern	rectilinear	rectilinear
External Fill Pattern	rectilinear	rectilinear
Interior Fill Percentage	100%	72%
Outline Overlap	15%	15%
Infill Extrusion Width	100%	100%
Minimum Infill Length	0mm	0 mm
Combine Infill Every	1 layer	1 layer
Include Solid Diaphragm Every	n/a	n/a
Internal Infill Angle Offsets	45 and -45	45 and -45
External Infill Angle Offsets	45 and -45	45 and -45
Support		
Generate Support Material	no	n/a
Support Extruder	Left Extruder (T0)	n/a
Support Infill Percentage	40%	n/a
Extra Inflation Distance	.5 mm	n/a
Support Base Layers	1	n/a
Combine Support Every	1 layer	n/a
Dense Support Extruder	Left Extruder (T0)	n/a
Dense Support Layers	0	n/a
Dense Infill Percentage	70%	n/a
Support Type	Normal	n/a
Support Pillar Resolution	1mm	n/a
Max Overhang Resolution	60 degrees	n/a
Horizontal Vertical Separation Layers	.3mm	n/a
Upper Vertical Separation Layers	1	n/a
Lower Vertical Separation Layers	1	n/a
Support Infill Angles	90	n/a

Table A.2: Printing parameters for conductive vs. non-conductive filament. Full profiles for conductive and non-conductive filament are in the 2nd appendix.

Parameter	Conductive Filament	Non-Conductive Filament
Temperature		
Left Extruder (T0)	160 C	150 C
Right Extruder (T1)	230 C	230 C
Heated Bed	65 C	65 C
Cooling		
Per-Layer Fan Controls	1:0, 2:100	2:100
Gcode		
GCode Section	left untouched	left untouched
Scripts		
Scripts	left untouched	left untouched
Speeds		
Default Printing Speed	1000 mm/min	3200 mm/min
Outline Underspeed	60%	60%
Solid Infill Underspeed	80%	80%
Support Structure Underspeed	80%	80%
X/Y Axis Movement Speed	3500 mm/min	4000 mm/min
z Axis Movement Speed	800 mm/min	1200 mm/min
Adjust Printing Speed for layers below	5 secs	5 secs
Allow Speed Reductions down to	40%	40%
Other		
Unsupported Area Threshold	5 sq. mm	5 sq. mm
Extra Inflation Distance	.15 mm	.15 mm
Bridging Extrusion Multiplier	90%	90%
Bridging Speed Multiplier	50%	50%
Used Fixed Bridging Infill Angle	n/a	n/a
Apply Bridging Settings to Perimeter	yes	yes
Horizontal Size Compensation	0 mm	0 mm
Filament Toolhead Index	tool 0	tool 0
Filament Diameter	1.75 mm	1.75 mm
Filament Price	35 price/kg	35 price/kg
Filament Density	1.25 grams/cm$\hat{3}$	1.25 grams/cm$\hat{3}$
Tool Change Retraction Distance	25 mm	25 mm
Tool Change Extra Restart Distance	.35 mm	.35 mm
Tool Change Retraction Speed	10000 mm/min	10000 mm/min

Table A.3: Printing parameters for conductive vs. non-conductive filament. Full profiles for conductive and non-conductive filament are in the 2nd appendix.

*P*arameter	Conductive Filament	Non-Conductive Filament
Advanced		
External Thin Wall Type	perimeters only	perimeters only
Internal Thin Wall Type	allow gap fill	allow gap fill
Allowed Perimeter Overlap	25%	25%
Minimum Extrusion Length	1 mm	1 mm
Minimum Printing Width	50%	50%
Maximum Printing Width	200%	200%
Endpoint Extension Distance	.2 mm	.2 mm
Only Retract When Crossing Open Spaces	no	no
Force Retraction Between Layers	no	no
Minimum Travel for Retraction	no	no
Perform Retraction During Wipe Movement	yes	yes
Only Wipe Extruder for Outer-Most Perimeters	yes	yes
Avoid Crossing Outline for Travel Movements	yes	yes
Maximum Allowed Detour Factor	10	10
Non-Manifold Segments	heal	heal
Merge All Outlines into a Single Solid Model	no	no

Table A.4: Printing parameters for conductive vs. non-conductive filament. Full profiles for conductive and non-conductive filament are in the 2nd appendix.

A.7 Copper and Nickel Plating Procedures

MTL	STANDARD OPERATING PROCEDURE	**Revision Number**	
		Version	1
		Approval Date	
		Review Date	

Changelog	**9/23/2022**	Document created.
Title	Procedure for Room-Temperature Metallization of Electroless Copper Plating	

Author	Nick Lubinsky	**Distribution**	General
Keywords	*Room-Temperature Metallization, Electroless Copper Plating*		

1. Summary

- This procedure outlined below will describe how to perform room-temperature metallization (RTM) of electroless copper plating. The process includes the methods to prepare parts to be plated as well as the plating process itself. In good conditions, the copper will deposit at 1.69 microns (0.067 mils) over 20 minutes of plating time.

2. Scope

- This procedure applies to the RTM electroless copper kit purchased from Transene® for the plating of ceramics, and other dielectric materials. Plating this way also extends to certain metals compatible with copper.

3. List of Equipment and Resources Required

- 3 beakers or vats large enough to fully submerge parts to be plated
- 1 additional beaker or vat **compatible with the etching solution used**
- Hot plate and magnetic stirrer
- Plastic or glass stirring rod
- Non-metallic tweezers or pliers
- Thermometer to monitor bath solution temperature

Applications

The RTM process is applicable to metallizing substrates in hybrid and microcircuits, insulated heat sinks, ceramic tubes, windows and terminals. Strong bond structures are produced. Structures with hermetic seals are formed as well.

The RTM process is also useful for metallizing barium titanate and ferrites. In addition, many polymeric materials, notably polyesters, epoxies, cellulosic, mylar and acrylonitrile-butadiene-styrene (ABS terpolymer) may be metallized following suitable modifications of the etch (Solution A).

RTM lends itself productively to the application of photolithographic technology using photoresist materials to register metallization patterns. In this manner, conductive pads may be formed for thin film and hybrid circuits. Base plates for building capacitor structures are also quite feasible.

Method of Plating

The RTM process involves first etching the surfaces of the part to be treated, to increase surface roughness and improve copper adhesion. This is material dependent, but usually involves an acid to partially dissolve the surface layers.

Post-etch, the part is sensitized and activated catalytically for the copper. This is done with palladium chloride, a tried-and-true activator.

Finally, the palladium acts as auto catalyst for the copper sulfate solution to reduce on. The copper will self-plate. Similarly for other metals. To reduce side reactions, the pH is kept Alkaline as it reduces.

4. Optional Etching Pre-treatment if Applicable

Before we begin plating, the parts to be plated must be prepared for the treatment. The first step is to determine whether the surface of these parts should be chemically etched. Etching increases surface roughness and improves adhesion of the copper layers during plating. Transene® recommends a surface roughness of about 20 microinches before plating. Consult the following for recommended etching pre-treatments based on material.

1. Solvent Decrease – Removes oil and grease; followed by vigorous water rinse.
2. Pumice Powder – Wet or dry, removes oxides, heavy soils (and/or vapor-blasting); followed by thorough water rinse.
3. Alkali Soak (5 Min) – Hot 150° to 180°F to further clean copper surface; condition laminate; improve surface wetting. Followed by warm water rinse.
4. Persulfate Etch (2 min) – Produces matte pink copper surface: ammonium persulfate – 200 gm/L; sulfuric acid – 10 ml/L. Followed by water rinse.
5. 10% Sulfuric Immersion (2 min) – Removes insoluble salts (Step #4). Followed by water rinse.
6. 33% HCL Immersion (2 min) – To protect from harmful drag-in.

Warning: Some etching components use dangerous caustics, such as hydrofluoric acid (HF). Consult the dedicated SOPs for those specific steps. This is only a general guide, with emphasis on the plating process itself.

COMPOSITION OF ETCH SOLUTIONS

Buffered Etch (Solution A) – a buffered solution **hydrofluoric acid**.

Chromic Acid

Chromium Trioxide	7.5 grams
Sulfuric Acid	25 mL
Water to	1 liter

Metal Etch

Nitric Acid	50% by volume
Glacial Acetic Acid	40% by volume
Water	10% by volume

Chromic-Sulfuric-HF- Solution

Chromium Trioxide	5% by volume
Sulfuric Acid	10% by volume
Hydrofluoric Acid (4896)	19% by volume

Stannous Chloride Solution

Stannous chloride 2% with hydrochloric acid added to obtain a clear solution.

5. PROCEDURE FOR RTM PROCESS

1. Preheat Electroless Copper Part A (blue copper-containing liquid) to desired operating temperature; 35 C produces good quality results.
2. Sensitizer Solution C (2 min. immersion) – Seeds epoxy/glass laminate. Followed by water rinse.
3. Activator Solution D (2 min. immersion) – Activates an autocatalytic layer for copper deposition. Followed by thorough water rinse.
4. 5% Sulfuric Dip (3-5 min. immersion) – Speeds electroless copper deposition, protects from drag-in contamination. Followed by water rinse.
5. Electroless Copper Parts A & B (60 min. typical) – Mix Electroless Copper Part B (clear liquid) into Part A, which has been preheated to operating temperature. Immerse part in plating bath and agitate slowly. Operate @ 30-45 °C. 35 C typically produces the best deposition, and 400 RPM agitation is sufficient. Follow by water rinse.
   Approx. Plating Rate: 5.08 microns (0.2 mils) per hour immersion time of optimally run plating. In practice, typically see faster plating deposition depending on copper content and temperature, among other factors.

   OPTIONAL – Follow up with electrolytic plating post-electroless copper immersion
6. 5% Sulfuric Dip – Neutralizes surface. Follow by water rinse.
7. 20% HCl Acid Dip (10-60 sec.) – Follow by water rinse.
8. Electroplate Copper – To build up desired copper thickness.

CARE OF RTM SOLUTION

Special Electroless Copper (Solution A) has an alkaline pH. This pH should not be allowed to drop below 7.0; although the solution is well buffered, the addition of sodium hydroxide from time to time may be required. The use of pH test paper is satisfactory for control.

Use at 30-45 °C (not over 50 °C). Bath should be held at optimum operation temperature of 40 °C for uniform plating thickness. Continuous mild agitation of work. Nominal plating rate 0.2 mil/hour. PC Electroless Copper is used for depositing thin layers of copper, up to 0.5 microns. For thicker films, Transene Copper Plating Acid Type should be used after initial electroless copper deposition. The copper content is 16 grams/gallon.

The electroless copper solution should be filtered to extend the usefulness of the solution whenever particles occur. The glass vessel used for RTM may sometimes develop a deposit of copper, due to overheating. The glass vessel should then be cleaned as well.

Sufficient quantities of RTM solutions should be used in the RTM Process. These used solutions, however, should not be returned to the original container to guard against contamination.

6. Training Plan and Measures of Competency

- If using any etching solution that contains any amount of hydrofluoric acid (HF), then the user is required to take MIT's specific HF course.

7. Work Health and Safety Considerations

- Any use of etching solutions, including HF, poses a safety hazard. Consult with the individual SOPs for those procedures.

8. References, Related Resources, and Acknowledgments

1. Transene Company, Inc.

9. Attachments or Related Documents

1. https://transene.com/rtm-process/
2. https://transene.com/cu/

STANDARD OPERATING PROCEDURE

Revision Number	
Version	1
Approval Date	
Review Date	

Changelog	**3/3/2022**	Document created.
	5/18/2022	Made steps more generalized.
Title	Procedure for Room-Temperature Metallization of Electroless Nickel Plating	

Author	Nick Lubinsky	**Distribution**	General
Keywords	*Room-Temperature Metallization, Electroless Nickel Plating*		

1. Summary

- This procedure outlined below will describe how to perform room-temperature metallization (RTM) of electroless nickel plating. The process includes the methods to prepare parts to be plated as well as the plating process itself. In good conditions, the nickel will deposit at 2.54 microns (0.1 mils) over 20 minutes of plating time.

2. Scope

- This procedure applies to the RTM electroless nickel kit purchased from Transene® for the plating of ceramics, and other dielectric materials. Plating this way also extends to certain metals compatible with nickel.

Room Temperature Metallizing for Alumina

Room-Temperature nickel metallizing process for alumina ceramics and other dielectric materials – strongly bonded nickel can be plated, soldered, brazed, or welded.

UNIQUE FEATURES

- Low-cost metallization process.
- Excellent bond strength – 100 psi typical.
- Withstands temperature extremes: – 65 °C. to + 850 °C.
- Passes Mil specifications for temperature cycling and shock.
- Hermeticity – leak rate < 10—8cc helium/second.
- Permits registration of metallization patterns with good resolution using photolithographic techniques and mechanical masking.
- Process applicable to beryllia, barium titanate, ferrites, epoxies, mylar and other dielectrics.

The nickel deposit is found to be unstressed, highly conductive, and extremely adherent with strong bond strength exhibited from –60 °C. to + 850 °C. It has a hardness of at least 500 (Vickers) as deposited. The adherent nickel deposit may be plated, soldered, brazed, or welded.

Applications

The RTM process is applicable to metallizing alumina substrates in hybrid and microcircuits, insulated heat sinks, ceramic tubes, windows and terminals. Strong bond structures are produced. Structures with hermetic seals are formed as well.

The RTM process is also useful for metallizing barium titanate and ferrites. In addition, many polymeric materials, notably polyesters, epoxies, cellulosic, mylar and acrylonitrile-butadiene-styrene (ABS terpolymer) may be metallized following suitable modifications of the etch (Solution A).

RTM lends itself productively to the application of photolithographic technology using photoresist materials to register metallization patterns. In this manner, conductive pads may be formed for thin film and hybrid circuits. Base plates for building capacitor structures are also quite feasible.

Method of Plating

The RTM process involves first etching the surfaces of the part to be treated, to increase surface roughness and improve nickel adhesion. This is material dependent, but usually involves an acid to partially dissolve the surface layers.

Post-etch, the part is sensitized and activated catalytically for the nickel. This is done with palladium chloride, a tried-and-true activator.

Finally, the palladium acts as auto catalyst for the nickel sulfate solution to reduce on. The nickel will self-plate. Similarly for other metals.

3. Determine Etching Pre-treatment if Applicable

Before we begin plating, the parts to be plated must be prepared for the treatment. The first step is to determine whether the surface of these parts should be chemically etched. Etching increases surface roughness and improves adhesion of the nickel layers during plating. Transene® recommends a surface roughness of about 20 microinches before plating. Consult the following table for recommended etching pre-treatments based on material.

Warning: Some etching components use dangerous caustics, such as hydrofluoric acid (HF). Consult the dedicated SOPs for those specific steps. This is only a general guide, with emphasis on the plating process itself.

SUBSTRATES	PRETREATMENT	ETCH	SENSITIZER & CONDITIONER	FIXING	NICKEL DEPOSITION OPER.TEMP.
Alumina	Polimet or Equivalent	Solution A	Solution B	Solution C	Solution D
Beryllia	“	HF (1 1/2 min)	“	“	65 °C
Magnesium Oxide	“	Chromic Acid (2 min.)	“	“	50 °C
Steatite	“	“	“	“	50 °C
Barium Titanate	“	Solution A (2 min.)	“	“	65 °C
Ferrites	“	HCl 20% (1 min.)	“	“	65 °C
Epoxies	“	Chromic Acid (3 min.)	“	“	45 °C
Mylar	“	Chromic Acid (3min.) followed with 25% KOH dip and rinse	“	“	45 °C
Polyethylene	“	“	“	“	45 °C
Polystyrene	“	“	“	“	45 °C
Lucite (Acrylic)	“		“	“	45 °C
Cellulose Acetate	“	Chromic Acid (2 min.)	“	“	45 °C
Lead Zirconate-Lead Titanate	“	Special*	“	“	90 °C

Applied to Lead Zirconate-Lead Titanate Pre-treatment*

1. Enough surface is required to obtain surface finish of 25-30 microinches average.
2. Soak in chromic-sulfuric HF solution 1 or 2 minutes, then rinse.
3. Soak in Solution A for 1 minute, then rinse.
4. Soak in potassium hydroxide 20% for l~ minutes. Rinse.
5. Soak in stannous chloride solution for 4 minutes. Follow by 1 mm. rinse in distilled or deionized water.
6. Continue RTM stops with steps III, IV, and V, using the solution B, C and D as indicated. Plate for 15 minutes.

COMPOSITION OF ETCH SOLUTIONS

Buffered Etch (Solution A) – a buffered solution **hydrofluoric acid**.

Chromic Acid

Chromium Trioxide	7.5 grams
Sulfuric Acid	25 mL
Water to	1 liter

Metal Etch

Nitric Acid	50% by volume
Glacial Acetic Acid	40% by volume
Water	10% by volume

Chromic-Sulfuric-HF- Solution

Chromium Trioxide	5% by volume
Sulfuric Acid	10% by volume
Hydrofluoric Acid (4896)	19% by volume

Stannous Chloride Solution

Stannous chloride 2% with hydrochloric acid added to obtain a clear solution.

4. List of Equipment and Resources Required

- 3 beakers or vats large enough to fully submerge parts to be plated
- 1 additional beaker or vat **compatible with the etching solution used**
- Hot plate and magnetic stirrer
- Plastic or glass stirring rod
- Non-metallic tweezers or pliers
- Thermometer to monitor bath solution temperature

5. Procedure

Detailed instructions are provided with each of the solutions used in the RTM process for alumina ceramics. For many other applicable materials, suitable etchants or process modifications are recommended. Steps 1 and 2 may be omitted as needed.

Etching, Sensitizing, and Fixing solutions should fully submerge the parts in question. Nickel plating solution (Solution D) used should form a bath whose volume is comparatively much larger than the part.

PROCEDURE FOR RTM PROCESS

1. **STEP I.** Preheat Electroless Nickel Deposition (Solution D) to optimum operating temperature of 90°C ready for use during the RTM Process (65°C with additive).

2. **STEP II.** Surface Pretreatment (Polimet)
The ceramic surface should exhibit surface roughness of at least 20 microinches, average, as shown by measurement with Brush Surf- indicator, Model MS-lOOO. If necessary, lap surface with Polimet to obtain adequate surface roughness of 25 microinches. Other means to obtain adequate surface roughness are applicable, E.G., sand- blasting. Polimet is used by converting it to a thin paste with water on a glass plate. The specimen is worked on the glass plate until the entire ceramic surface appears uniformly lapped. Rinse well in water to remove lapping compound.

3. **STEP III.** Etch (Solution A) Place the lapped ceramics in the appropriate buffered etch solution from the chart above (**CAUTION! Solution A contains HF**. If using it, Solution A **must** be contained in a polyethylene beaker), for the time listed in the same chart. Finally remove ceramic pieces from the etch solution and rinse thoroughly in water.

4. **STEP IV.** Surface Sensitizing (Solution B) Expose etched ceramics to Solution B for 4 minutes. Do not stir or agitate the solution. Avoid contamination from metal objects. Use glassware and plastic-coated tweezers or transfer racks for handling. Remove surface-sensitized ceramics, and without rinsing transfer the ceramics to the next solution. Solution contains palladium chloride, activating the nickel plating process.

5. **STEP V.** Fixing (Solution C) The ceramics should be allowed to stand in Solution C for 4 minutes. Again, do not agitate or stir. Finally remove ceramics and carefully rinse in distilled or deionized water by limiting the water rinse to a maximum of 30 seconds. Transfer to next step immediately.

6. **STEP VI.** Electroless Nickel Deposition (Solution D) must be held at optimum operating temperature of 90°C ready for use during the RTM Process. Addition of 12 gm/gal dimethylamine borane (Solution D Additive) prior to using Solution D is an effective means of lowering the plating temperature to 65°C. The ceramic pieces are placed in this special electroless nickel solution without agitation for first few minutes.
Approx. Plating Rate: 7.62 microns (0.3 mils) per hour immersion time of optimally run plating

CARE OF RTM SOLUTION

Special Electroless Nickel (Solution D) has a pH of 8.0. This pH should not be allowed to drop below 7.0; although the solution is well buffered, the addition of ammonium hydroxide from time to time may be required. The use of pH test paper is satisfactory for control.

The electroless nickel solution should be filtered to extend the usefulness of the solution whenever particles occur. The glass vessel used for RTM may sometimes develop a deposit of nickel, due to overheating. The glass vessel should then be cleaned as well.

Sufficient quantities of RTM solutions should be used in the RTM Process. These used solutions, however, should not be returned to the original container to guard against contamination.

6\. **STEP VII.** Once desired thickness is achieved, finally remove ceramics and rinse in water.

6. Training Plan and Measures of Competency

- If using any etching solution that contains any amount of hydrofluoric acid (HF), then the user is required to take MIT's specific HF course.

7. Work Health and Safety Considerations

- Any use of etching solutions, including Transene Solution A, poses a safety hazard. Consult with the individual SOPs for those procedures.

8. References, Related Resources, and Acknowledgments

1. Transene Company, Inc.

9. Attachments or Related Documents

1. https://transene.com/rtm-process/

A.8 Circuitry List

1. RLC Transformer Board
    - 332G-NA5880-AE Coupled Inductor (1:4 voltage step-up and 12MHz SRF)
    - 7M3-333 variable inductor (33uH nominal 25-41uH)
    - MOS6020-473ML (47 uH)
    - MOS6020-154ML (150uH)
    - CER 12PF 200V C0G/NP0 0402
    - RES 10 OHM 1% 45W TO252
2. Main ESP32 Board combined with Full-Bridge and Buffer Circuit
    - RX TXRX MOD WIFI TRACE ANT SMD (1965-ESP32-WROOM-32D-N16CT-ND)
    - 100V HALF BRIDGE DRIVER W/ FLOAT (LTC7060)
    - CAP CER 10UF 16V X7R 1206
    - CAP CER 1.8UF 50V X7R 1206
    - CAP CER 1UF 50V X7R 1206
    - CAP CER 0.1UF 50V X7R 1206
    - DIODE SCHOTTKY 100V 1A DO214AA (641-1104-1-ND)
    - DIODE SCHOTTKY 30V 200MA SOD323 (1514-CMDSH2-3TRPBFREECT-ND)
    - MOSFET N-CH 200V 34A D2PAK (IPB320N20N3GATMA1CT-ND)
    - FET RF 30V 520MHZ PLD (AFT05MS004NT1CT-ND)
    - RF TRANS NPN 25V 650MHZ SOT23-3 (KST10MTFCT-ND)
    - IC OPAMP JFET 1 CIRCUIT 8SOIC (296-OPA810IDRCT-ND)
    - IC REG LINEAR 3.3V 1A SOT223 (ZLDO1117G33DICT-N)

  - CONN HEADER SMD R/A 11POS 2.54MM
  - SWITCH TACTILE SPST-NO 0.05A 24V
  - SWITCH SLIDE SPDT 100MA 12V (401-2012-1-ND)
  - 1 Cermant 2000 psc 1206 SMD Resistor Kit

3. TPS55289 Buck-Boost Converter Evaluation Board
4. MG Chemicals 8331D Silver Conductive Epoxy Adhesive, High Conductivity, 20 min Working time, 2-Part, 14 Gram Kit
5. USB to TTL Serial 3.3V UART Converter Cable with FTDI Chip Terminated by 6 Way Header